

Cover Page



Universiteit Leiden

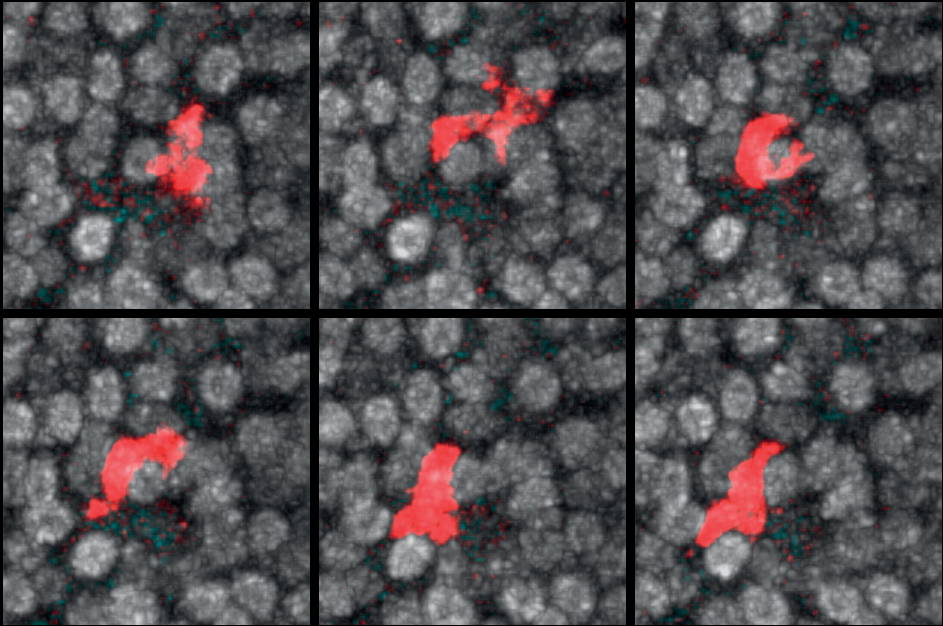


The handle <http://hdl.handle.net/1887/138854> holds various files of this Leiden University dissertation.

**Author:** Dijkgraaf, F.E.

**Title:** T cells in focus: Formation and function of tissue-resident memory

**Issue date:** 2021-01-12



# Chapter 8

## Tissue patrol by resident memory CD8<sup>+</sup> T cells in human skin

Feline E Dijkgraaf<sup>1</sup>, Tiago R Matos<sup>2,\*</sup>, Mark Hoogenboezem<sup>3,\*</sup>, Mireille Toebes<sup>1</sup>, David W Vredevoogd<sup>1</sup>, Marjolijn Mertz<sup>4</sup>, Bram van den Broek<sup>4</sup>, Ji-Ying Song<sup>5</sup>, Marcel BM Teunissen<sup>2</sup>, Rosalie M Luiten<sup>2</sup>, Joost B Beltman<sup>6</sup> and Ton N Schumacher<sup>1,#</sup>

*Nature Immunology*, 2019, Jun, 20(6):756-764. doi: 10.1038/s41590-019-0404-3

<sup>1</sup> Division of Molecular Oncology & Immunology, OncoCode Institute, The Netherlands Cancer Institute, Amsterdam, The Netherlands

<sup>2</sup> Department of Dermatology and Netherlands Institute for Pigment Disorders, Amsterdam University Medical Centers, University of Amsterdam, The Netherlands

<sup>3</sup> Research Facility, Sanquin Amsterdam, The Netherlands

<sup>4</sup> Bioluminescence Imaging Facility, The Netherlands Cancer Institute, Amsterdam, The Netherlands

<sup>5</sup> Animal Pathology, The Netherlands Cancer Institute, Amsterdam, The Netherlands

<sup>6</sup> Division of Drug Discovery and Safety, Leiden Academic Centre for Drug Research, Leiden University, Leiden, The Netherlands

\* These authors contributed equally to this work

# To whom correspondence should be addressed: t.schumacher@nki.nl

**ABSTRACT**

Emerging data show that tissue-resident memory T cells ( $T_{RM}$ ) play an important protective role at murine and human barrier sites. Mouse skin- $T_{RM}$  cells in the epidermis patrol their surroundings and rapidly respond upon antigen encounter. However, whether a similar migratory behavior is performed by human  $T_{RM}$  cells is unclear, as technology to longitudinally follow them *in situ* has been lacking. To address this issue, we developed an *ex vivo* culture system to label and track T cells in fresh skin samples. We validated this system by comparing *in vivo* and *ex vivo* properties of murine  $T_{RM}$  cells. Using nanobody labeling, we subsequently demonstrate in human *ex vivo* skin that  $CD8^+$   $T_{RM}$  cells migrated through the papillary dermis and the epidermis, below sessile Langerhans cells. Collectively, this work allows the dynamic study of resident immune cells in human skin and demonstrates the existence of tissue patrol by human  $CD8^+$   $T_{RM}$  cells.

## INTRODUCTION

Tissue-resident memory T cells (T<sub>RM</sub>) are non-circulating lymphocytes that play a key role in peripheral immunity. T<sub>RM</sub> cells have been described in both mouse and human tissues such as lung, intestine, brain and skin<sup>1,2,3,4</sup> and show a transcriptional profile that is, among others, characterized by CD69 expression and in some tissues also CD103 expression<sup>5,6,7</sup>. The T<sub>RM</sub> cells that reside at peripheral sites orchestrate immune responses against pathogens, but also contribute to autoimmune and allergic disorders<sup>4,8,9,10</sup>. Furthermore, CD103<sup>+</sup> T cells are present in human cancer lesions such as melanoma<sup>11</sup>, ovarian<sup>12</sup> and lung cancer<sup>13,14</sup>, are enriched in tumor reactivity<sup>15</sup> and are therefore thought to play a central role in tumor control.

Intravital imaging studies in mouse models have demonstrated that CD8<sup>+</sup> T<sub>RM</sub> cells in skin tissue actively crawl in between keratinocytes in search of newly infected cells, a property termed tissue patrol<sup>16,17</sup>. Encounter of antigen-expressing cells by T<sub>RM</sub> cells in mouse models is accompanied by a reduction in their motility and dendricity, as revealed by *in vivo* imaging<sup>16,18,19</sup>. Furthermore, antigen encounter by CD8<sup>+</sup> T<sub>RM</sub> cells induces the tissue-wide expression of interferon- (IFN- $\gamma$ ) responsive genes, as for instance demonstrated by transcriptional analyses<sup>20,21</sup>.

While there is a growing appreciation of the relevance of human skin-resident T<sub>RM</sub> cells in health and disease<sup>4,22</sup>, the *in situ* behavior of these cells has not been analyzed. To address this issue, we set out to develop an *ex vivo* tissue culture system to study the dynamic behavior of T<sub>RM</sub> cells in fresh skin biopsies. We first validated this system on mouse tissue by comparison of *in vivo* and *ex vivo* T<sub>RM</sub> cell migration and antigen recognition by *ex vivo* T<sub>RM</sub> cells. We subsequently determined how T<sub>RM</sub> cells in fresh biopsy material can be visualized by staining with fluorescent anti-CD8 nanobodies, without impairing their ability to respond to antigen encounter. We then applied this approach to healthy human skin samples and demonstrate that human CD8<sup>+</sup> skin-resident T<sub>RM</sub> cells migrated in both the epidermal and dermal compartment. In the epidermal compartment, CD8<sup>+</sup> T<sub>RM</sub> cells moved along the stratum basale, in close proximity to the basement membrane, and below a pool of stationary Langerhans cells. In the papillary dermis, migration of CD8<sup>+</sup> T<sub>RM</sub> cells in both collagen type I-dense regions and in collagen type I-poor areas along dermal vessels was observed. This study demonstrates that tissue patrol is a property of human tissue-resident memory CD8<sup>+</sup> T cells and provides a platform to study the real-time behavior of these cells *in situ*.

## RESULTS

### ***Ex vivo* migration of murine CD8<sup>+</sup> T<sub>RM</sub> cells in skin tissue**

In order to study human skin-resident T<sub>RM</sub> cell behavior in real-time, we aimed to set up a skin culture system suitable for live-cell imaging. To this end, we explored an *ex vivo* culture

system previously used to image melanoblast migration<sup>23</sup> to investigate whether  $T_{RM}$  cell behavior in such an *ex vivo* system recapitulates *in vivo* cell behavior. In this setup, a fresh skin biopsy is mounted between a gas-permeable membrane at the epidermal side and a filter covered by matrigel and medium on the dermal side (**Fig. 1a**). This system ensures gas exchange at the exterior side of the skin, while providing diffusion of nutrients on the interior side.

To examine whether such an *ex vivo* imaging system can be used to reliably describe properties of skin-resident  $T_{RM}$  cells, we first compared *ex vivo*  $T_{RM}$  cell migration to the well-understood migratory behavior of mouse skin-resident  $T_{RM}$  cells *in vivo*<sup>16, 17</sup>. To this end, mice harboring fluorescently labeled skin-resident  $T_{RM}$  cells were generated by injection of naïve OT-I T cell antigen receptor (TCR)-transgenic  $CD8^+$  T cells, specific for the ovalbumin-derived SIINFEKL peptide (OVA<sub>257-264</sub>), that express green fluorescent protein (GFP), into C57BL/6 mice followed by DNA vaccination on skin of both hindlegs with a plasmid encoding the OVA<sub>257-264</sub> epitope (experimental setup in **Fig. 1b**). >44 days after induction of a local T cell response, the migration of tissue-resident T cells was analyzed by *in vivo* confocal microscopy. Subsequently, skin of the same animals was harvested, mounted for *ex vivo* imaging, and analyzed by longitudinal (4 h) confocal the next day. *In vivo* GFP<sup>+</sup> skin-resident  $T_{RM}$  cells displayed the previously described dendritic morphology and constantly migrated within the tissue with a median speed of  $0.49 \pm 0.29 \mu\text{m}/\text{min}$  (**Fig. 1c**, top and bottom, and **Supplementary Video 1**). Imaging of *ex vivo* skin showed that GFP<sup>+</sup> skin-resident  $T_{RM}$  cells remained present within the epidermis and largely retained their dendritic shape (median circularity of  $0.38 \pm 0.06$  and  $0.42 \pm 0.03$  for *in vivo* and *ex vivo* skin-resident  $T_{RM}$  cells respectively, whereby a value of 1.0 represents a fully circular morphology; **Fig. 1c**, top middle and bottom right). Furthermore, *ex vivo* skin-resident  $T_{RM}$  cells also retained their constitutive migratory behavior, with a slightly higher median speed of  $0.68 \pm 0.70 \mu\text{m}/\text{min}$  (**Fig. 1c**, bottom left and **Supplementary Video 2**). Notably, gas exchange in this *ex vivo* system was crucial to retain physiological skin-resident  $T_{RM}$  cell behavior, as mounting of murine skin in a setup in which gas exchange is prevented resulted in highly immobile (median speed of  $0.08 \pm 0.04 \mu\text{m}/\text{min}$ ) and circular (median circularity of  $0.72 \pm 0.01$ ) GFP<sup>+</sup> skin-resident  $T_{RM}$  cells (**Fig. 1c**, top right and bottom, and **Supplementary Video 3**). Analysis of migration parameters revealed that *ex vivo* skin-resident  $T_{RM}$  cells displayed a higher motility coefficient than *in vivo*  $T_{RM}$  cells, as indicated by non-overlapping confidence intervals (**Supplementary Fig. 1a**, left). Nonetheless, persistence time and median turning angles were very comparable (**Supplementary Fig. 1a**, middle and right). Prior work has demonstrated that intravital imaging of pigmented skin can induce a local immune response due to death of light-sensitive pigmented skin cells and subsequent recruitment of neutrophils<sup>24, 25, 26</sup>. To study whether the observed T cell behavior could indeed be influenced by death of pigment-positive skin cells, we performed *in vivo* and *ex vivo* confocal imaging of  $T_{RM}$  cells in skin of C57BL/6 albino mice. These data demonstrate that the steady-state patrolling behavior of skin-resident  $T_{RM}$

cells was independent of the presence of skin pigmentation (**Supplementary Fig. 1b**, top and bottom left and middle, and **Supplementary Video 4**). In addition, the typical T<sub>RM</sub> cell patrolling behavior observed in confocal imaging, was also seen during multiphoton (MP) imaging of GFP<sup>+</sup> OT-I T<sub>RM</sub> cells in skin of C57BL/6 albino mice (**Supplementary Fig. 1b**, top and bottom right, and **Supplementary Video 5**). In further support of the notion that steady state migration is an intrinsic property of skin-resident T<sub>RM</sub> cells, mean speeds remained constant over long-term confocal and MP imaging periods in skin of C57BL/6 black and albino animals (**Supplementary Fig. 1c**).

Having demonstrated that *ex vivo* skin-resident T<sub>RM</sub> cells retain their steady state migratory behavior, we next examined whether these cells could still respond to cognate antigen encounter. To address this, mice harboring a mixture of red-fluorescent (mTmG) OVA<sub>257-264</sub>-specific and green-fluorescent (GFP) Herpes simplex virus (HSV) gB<sub>498-505</sub>-specific skin-resident T<sub>RM</sub> cells were generated by vaccination with vectors encoding these epitopes, thereby allowing the subsequent comparison of the behavior of these two populations during *ex vivo* recall with one of the two antigens. After a >60-day rest period, skin tissue was harvested and mounted for *ex vivo* imaging. Consistent with the data in Fig. 1c, *ex vivo* OT-I-mTmG and gBT-GFP skin-resident T<sub>RM</sub> cells exhibited a dendritic morphology and continuously crawled within the tissue in steady state (**Fig. 1d** left and **Supplementary Fig. 1d**). However, upon addition of OVA<sub>257-264</sub> peptide to the *ex vivo* medium, OT-I-mTmG cells rounded up and stalled, with a 4-fold reduction in median speed, whereas gBT-GFP cells remained dendritic and motile throughout the recording (**Fig. 1d**, right, **Supplementary Fig. 1d** and **Supplementary Video 6**). Together, these data demonstrate that this *ex vivo* imaging system recapitulates key aspects of *in vivo* T<sub>RM</sub> cell behavior and can hence be used to study skin-resident T<sub>RM</sub> cells in real-time in settings where *in vivo* imaging is precluded.

### **Ex vivo labeling with anti-CD8 nanobody allows visualization and tracking of CD8<sup>+</sup> murine skin-resident T<sub>RM</sub> cells**

In order to visualize the behavior of human CD8<sup>+</sup> skin-resident T<sub>RM</sub> cells *in situ*, it was necessary to develop a means to label T<sub>RM</sub> cells *ex vivo*. To ensure efficient tissue penetration by fluorescently labeled antibodies in the relatively thick human skin<sup>27</sup>, we generated ±15 kDa-sized Alexa Fluor-594 (AF594)-labeled nanobodies against both mouse (m) and human (h) CD8 molecules (hereafter referred to as anti-mCD8 and anti-hCD8 nanobodies, respectively). Subsequently, *ex vivo* staining of murine skin harboring CD8<sup>+</sup> GFP<sup>+</sup> skin-resident T<sub>RM</sub> cells was utilized to validate the use of these reagents. *Ex vivo* imaging of tissue stained with anti-mCD8 nanobody demonstrated successful labeling of all GFP<sup>+</sup> cells within the tissue (**Fig. 2a**, left), and this signal remained constant over time (**Fig. 2a**, top right). In addition, a population of endogenous, non-GFP-transgenic, tissue-resident CD8<sup>+</sup> cells was detected, as revealed by the presence of single AF594-positive cells (indicated with asterisk). As a control, staining of mouse skin explants with AF594-nanobody reactive with human CD8

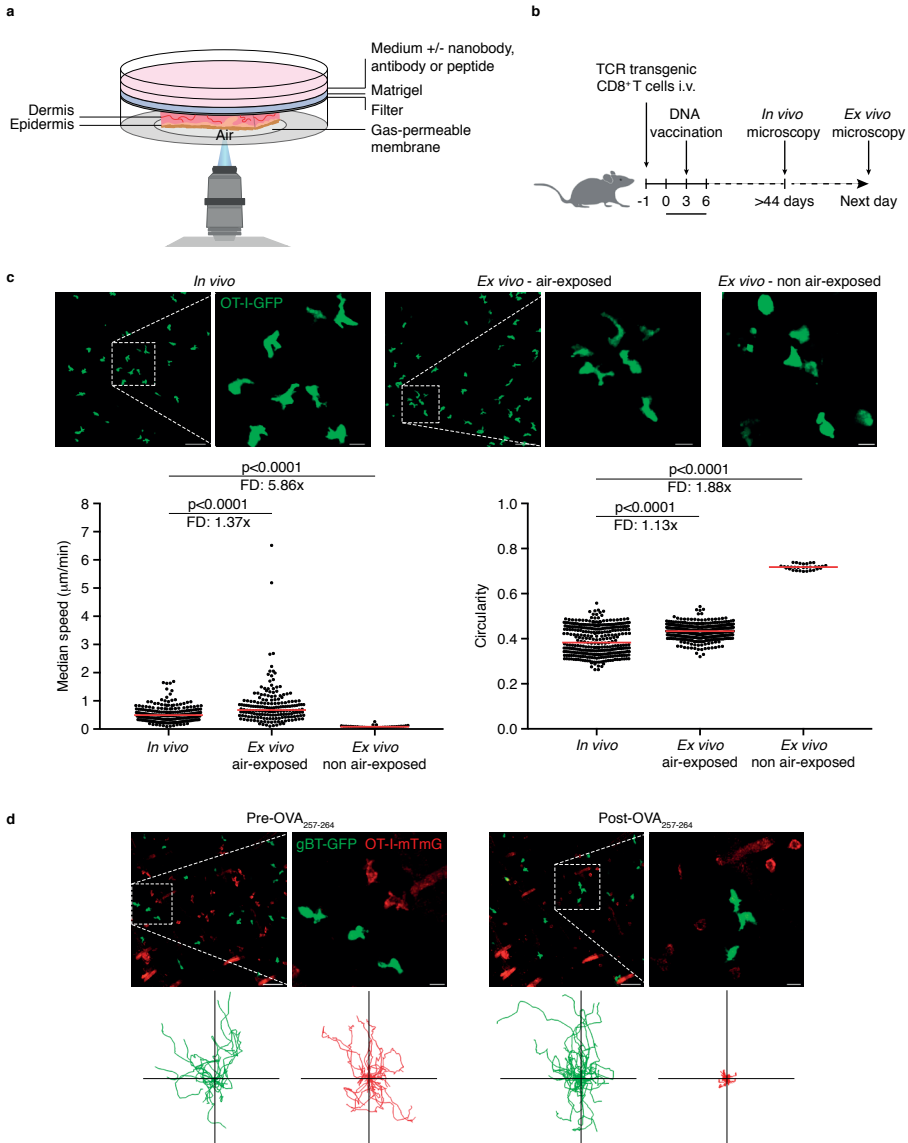
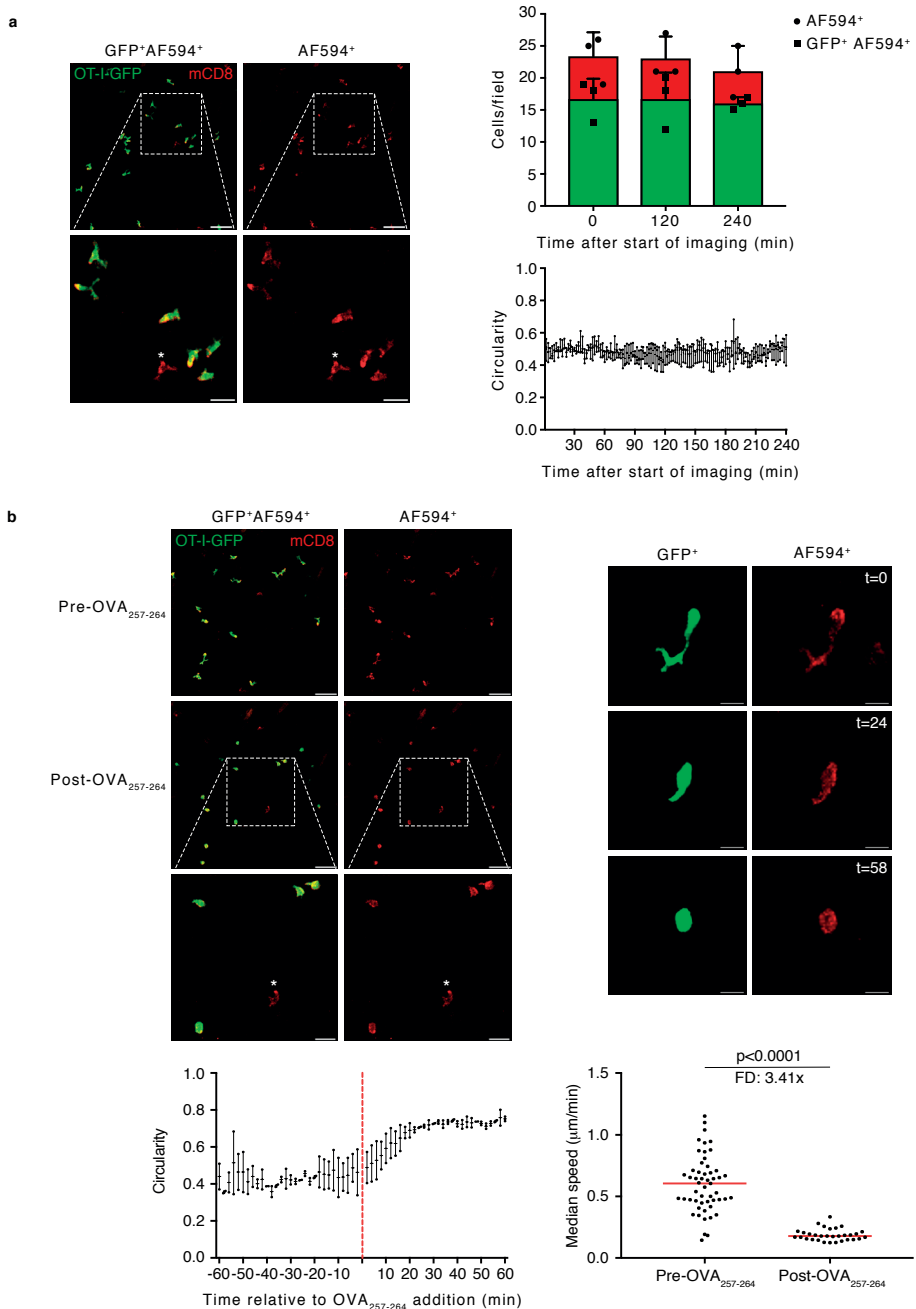


**Figure 1 | Tissue patrol and cognate antigen recognition by ex vivo murine skin-resident T<sub>RM</sub> cells.** **a**, Illustration of ex vivo skin imaging setup. **b**, Experimental setup to compare in vivo and ex vivo skin-resident T<sub>RM</sub> cell behavior. **c**, Top: confocal maximum intensity projections of in vivo (left, overview and zoomed image), ex vivo air exposed (middle, overview and zoomed image) and ex vivo non air exposed (right, zoomed image) OT-I-GFP (green) cells. Bottom: in vivo (left, median speed, n=217; right, circularity, n=342), ex vivo air exposed (left, median speed, n=185; right, circularity, n=364) and ex vivo non air exposed (left, median speed, n=33; right, circularity, n=31) skin-resident T<sub>RM</sub> cells. Black dots represent medians of individual tracks of T<sub>RM</sub> cells (left) or average T<sub>RM</sub> cell circularity per frame (right), red lines indicate median of cell population, FD indicates fold difference. Two-tailed Mann-Whitney U-tests were performed. In vivo and ex vivo with gas exchange data are representative of n=3 mice per condi-

tion (4 h recordings), *ex vivo* without gas exchange data are based on n=1 (1 h recording). **d.** Confocal maximum intensity projections (overview and zoomed image) of OT-I-mTmG (red) and gBT-GFP (green) cells before (top left) and after (top right) OVA<sub>257-264</sub> addition. Note that, next to red fluorescent T cells, autofluorescent hair fragments are visible in the red channel. Bottom: individual tracks of cells in 1 h- (pre) and 2 h- (post) recordings after normalization of starting positions to the origin. Data are representative of 3 mice. Scale bars indicate 50  $\mu\text{m}$  and 10  $\mu\text{m}$  for overviews and zoomed images, respectively.

did not result in specific staining (**Supplementary Fig. 2a**). Staining of *ex vivo* mouse skin with anti-mCD8 nanobody did not lead to a substantial change in morphology of CD8<sup>+</sup> GFP<sup>+</sup> cells (**Fig. 2a**, bottom right). Furthermore, nanobody-labeled skin-resident T<sub>RM</sub> cells retained a continuous crawling behavior with similar median speeds ( $0.82 \pm 0.58 \mu\text{m}/\text{min}$ , **Supplementary Fig. 2b**, top left). Analysis of migration parameters showed a 1.3-fold decrease in median turning angles following nanobody labeling, whereas motility coefficient and persistence time were very comparable to non-labeled *ex vivo* skin-resident T<sub>RM</sub> cells, as indicated by overlapping confidence intervals (**Supplementary Fig. 2b**, top right and bottom). Interestingly, in the majority of the cells, the highest intensity of CD8 staining was observed on the lagging end of migrating skin-resident T<sub>RM</sub> cells (**Supplementary Fig. 2c**). Because of the monovalency of the labeled nanobodies, this is not expected to be a consequence of labeling-induced receptor clustering and may therefore represent a physiological enrichment at this site.

To understand at which time scales *ex vivo* culture would affect tissue integrity, we performed histopathological analysis of *ex vivo* cultured tissue fixed at different time points after mounting. Nanobody-labeled *ex vivo* tissue that was imaged for a 4 h time period one day after mounting showed only mild degeneration and mild hypertrophic change of the epidermal squamous cells, and overall skin integrity was maintained (**Supplementary Fig. 2d**, top). Langerhans cells have been described to leave tissues under stress conditions<sup>28</sup> and, as a second measure for tissue stress, we performed staining of Langerhans cells in *ex vivo* tissue that was fixed at various time points after mounting. This revealed that Langerhans cells remained present *ex vivo* up to 72 h in culture (**Supplementary Table 1**). In addition, large numbers of GFP<sup>+</sup> skin-resident T<sub>RM</sub> cells were still observed at this time point (**Supplementary Fig. 2d**, bottom). In order to examine whether labeling of T<sub>RM</sub> cells with anti-mCD8 nanobody would influence their ability to recognize cognate antigen, OVA<sub>257-264</sub> peptide was added to medium of GFP<sup>+</sup> OT-I T<sub>RM</sub> cells harboring *ex vivo* skin that was labeled with anti-mCD8 nanobody. After addition of peptide ligand, CD8<sup>+</sup> GFP<sup>+</sup> AF594<sup>+</sup> cells showed a 3.4-fold reduction in median speed and became highly circular in less than 30 min, indicating response to antigen encounter (**Fig. 2b**, left and bottom, and **Supplementary Video 7**). As a side note, the previously enriched mCD8 signal at the rear side of patrolling cells appeared redistributed over the cell surface upon antigen delivery (**Fig. 2b**, top right). While all GFP<sup>+</sup> AF594<sup>+</sup> cells stalled after peptide addition, isolated dendritic single positive AF594<sup>+</sup> cells were observed that continued to migrate after OVA<sub>257-264</sub> peptide addition, suggesting



GFP<sup>+</sup> AF594<sup>+</sup> double positive and AF594<sup>+</sup> single positive cells at different time points after start of the recording. Bar graph shows mean plus SD and individual data points. Bottom right: circularity of anti-mCD8 nanobody labeled GFP<sup>+</sup> cells over time. Data are based on 4h recordings of n=3 mice. **b**, Top left: confocal maximum intensity projections of *ex vivo* anti-mCD8 labeled skin-resident T<sub>RM</sub> cells, before (top) and after (middle, bottom) OVA<sub>257-264</sub> addition. Note that the sole AF594 single positive cell remains dendritic. Top right: illustration of kinetics of morphology change of a GFP<sup>+</sup> AF594<sup>+</sup> cell upon *ex vivo* OVA<sub>257-264</sub> addition (time in minutes, peptide addition at t=0). Bottom left: circularity of GFP<sup>+</sup> cells before and after OVA<sub>257-264</sub> addition (indicated with dashed red line). Bottom right: black dots indicate median speeds of individual tracks pre- (n=53) and post- (n=31) antigen delivery, with red lines indicating median of all cells. FD indicates fold difference. A two-tailed Mann-Whitney U-test was performed. Data are representative of n=2 mice and 2 h recordings. Scale bars indicate 50 μm and 10 μm for overviews and zoomed images, respectively. Circularity graphs show min-max (lines), individual data points (dots), and the mean (plus-symbol).

that these endogenous cells recognized a distinct epitope. While antigen recognition by T<sub>RM</sub> cells was not affected by nanobody labeling in these settings, such labeling could potentially affect TCR triggering at lower antigen concentrations. Analysis of *in vitro* cytokine production by anti-mCD8 nanobody-labeled mouse T cells revealed a reduction in antigen sensitivity of approximately 10-fold (**Supplementary Fig. 2e**). Notably, staining of human T cells with anti-hCD8 nanobody did not measurably influence their antigen sensitivity or the recognition of tumor cells that endogenously expressed the cognate antigen (**Supplementary Fig. 3a**).

Collectively, these data demonstrate that *ex vivo* imaging of CD8<sup>+</sup> skin-resident T<sub>RM</sub> cells is feasible, that these cells retain their physiological tissue patrolling behavior, and that such cells can efficiently be labeled with nanobodies *in situ*.

### Migratory behavior of human CD8<sup>+</sup> skin-resident T<sub>RM</sub> cells

Memory T cells have been observed in healthy human skin, with numbers remaining stable up to 90 years of age<sup>4</sup>. Contrary to T cells present in skin during ongoing infections, T cells present in healthy skin tissue are likely to represent resident memory cells as revealed by expression of CD45RO, CLA and CD69<sup>29, 30</sup>. To study the behavior of these cells *in situ*, we mounted punch biopsies of skin material obtained after abdominoplastic or breast reconstructing surgery for *ex vivo* imaging and stained these tissues with anti-hCD8 nanobody. Multiphoton microscopy (MP) the next day revealed specific staining of CD8<sup>+</sup> cells in human skin, as compared to staining with irrelevant anti-mCD8 (**Fig. 3a**). To investigate the localization of CD8<sup>+</sup> cells in human skin samples, tissues were also incubated with the nuclear dye Hoechst, to show the distribution of all nucleated cells in these samples. This imaging revealed a subpopulation of CD8<sup>+</sup> cells that was preferentially located in the stratum basale of the epidermis (**Fig. 3b**, left). In addition, imaging of collagen type I by second harmonic generation (SHG) signal showed the presence of sizable numbers of CD8<sup>+</sup> cells in the papillary dermis (**Fig. 3b**, middle and right). To assess whether the observed dermal and epidermal cell populations both reflected resident memory T cells, we analyzed expression

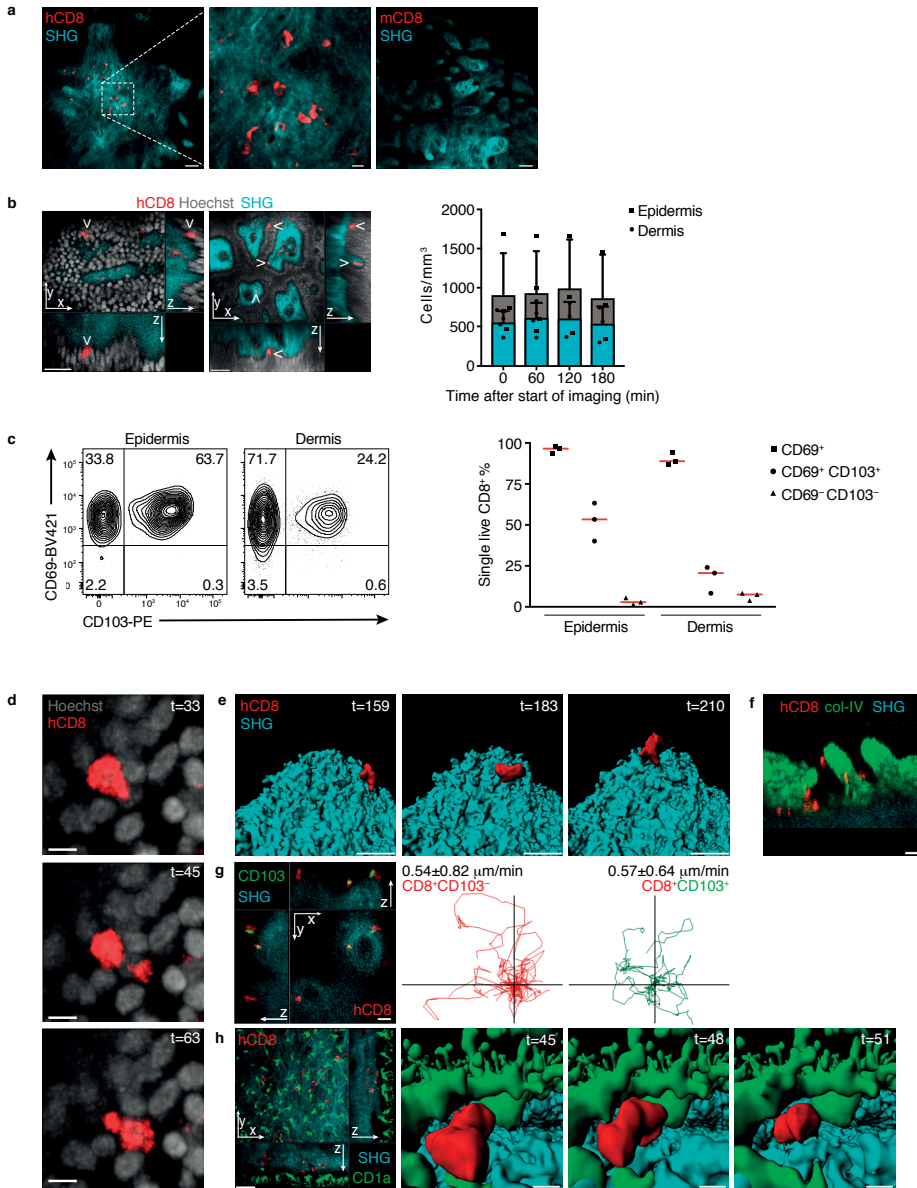


**Figure 3 | Migratory properties of CD8<sup>+</sup> T<sub>RM</sub> cells in human epidermis.** **a**, Multiphoton (MP) maximum intensity projections of *ex vivo* human skin stained with anti-hCD8-AF594 (left and middle, red, representative of *n*=4 individuals) or control anti-mCD8-AF594 (right, red, representative of *n*=3 individuals). Scale bars indicate 50  $\mu$ m and 10  $\mu$ m for overviews and zoomed images, respectively. Second harmonics signal (SHG) represents dermal collagen type I (blue). **b**, Left: virtual sectioning of MP images of *ex vivo* anti-hCD8 (red) and Hoechst 33342 (nuclei, grey) stained biopsy (SHG, blue). '>' indicate CD8<sup>+</sup> cells and scale bars represent 50  $\mu$ m. Right: quantification of AF594<sup>+</sup> cells in indicated compartments over time. Data is representative of *n*=4 individuals. Bar graphs show mean plus SD and

individual data points. **c**, Flow cytometric analysis of indicated single cell suspensions. Cells are gated on single/live/CD8<sup>+</sup> lymphocytes (n=3 individuals). Right: black symbols indicate individuals, red line indicates median. **d**, MP maximum intensity projection of Hoechst<sup>+</sup> hCD8<sup>+</sup> cell (grey and red) migrating in between Hoechst<sup>+</sup> nuclei (representative of n=4 individuals). **e**, 3D-surface rendering of MP recording of epidermal hCD8<sup>+</sup> cell (red) migrating on top of dermal papillae (SHG, blue). **f**, Orthogonal view of MP recording showing CD8<sup>+</sup> (red) cells in close proximity to collagen type IV positive basement membrane (green) (SHG, blue) (representative of n=3 individuals). **g**, Left: virtual sectioning of MP recording (left) and pooled track plots (right) of epidermal CD8<sup>+</sup> (red) and CD8<sup>+</sup>CD103<sup>+</sup> (red + green) cells (SHG, blue) (representative of n=3 individuals). Scale bars in Fig. 3d-g indicate 20  $\mu$ m. **h**, Left: virtual sectioning of MP recording of anti-hCD1a (green) plus anti-hCD8 (red) stained biopsy (SHG, blue). Scale bar indicates 50  $\mu$ m. Right three images: 3D surface rendering of CD8<sup>+</sup> cell migrating in close proximity to CD1a<sup>+</sup> Langerhans cells (representative of n=4 individuals). Scale bars indicate 10  $\mu$ m.

of CD69 and CD103 on CD8<sup>+</sup> cells isolated from the dermal and epidermal layer, revealing CD69 positivity on nearly all CD8<sup>+</sup> cells in both compartments, and with a large fraction of cells also expressing CD103 (**Fig. 3c**). In addition, this analysis revealed that the *in situ* labeling of CD8<sup>+</sup> T cells identifies the entire CD8<sup>+</sup> T cell compartment present in these skin biopsies, as determined by co-staining of single cell suspensions of *in situ* labeled cells with conventional anti-CD8 antibody following digestion (**Supplementary Fig. 3b**).

Long term MP imaging of human skin stained with anti-hCD8 revealed that CD8<sup>+</sup> T<sub>RM</sub> cells migrated in the epidermal and dermal compartment, with speeds remaining constant throughout MP imaging sessions (**Supplementary Video 8** and **Supplementary Fig. 3c**). Co-staining of *ex vivo* tissues with anti-hCD8 and the nuclear dye Hoechst revealed that CD8<sup>+</sup> T<sub>RM</sub> cells in the epidermal compartment migrated in the stratum basale, through a dense environment of keratinocytes (**Fig. 3d** and **Supplementary Video 9**). In contrast to the CD8<sup>+</sup> skin-resident T<sub>RM</sub> cells observed in mouse epidermis, human epidermal CD8<sup>+</sup> T<sub>RM</sub> cells did not only migrate primarily in 2D but followed the 3D structure of the finger-like dermal projections (**Fig. 3e** and **Supplementary Video 10**). Migration of epidermal T<sub>RM</sub> cells in close proximity to the basement membrane (BM) could likewise be revealed by co-staining with an antibody for collagen type IV (col-IV) that forms one of the major BM components<sup>31</sup> (**Fig. 3f** and **Supplementary Video 10**). As only a fraction of human epidermal CD8<sup>+</sup> T<sub>RM</sub> cells also expresses CD103, we next investigated the location and motility of the CD8<sup>+</sup>CD103<sup>-</sup> and CD8<sup>+</sup>CD103<sup>+</sup> T<sub>RM</sub> cell subsets. To this end, we co-stained tissue explants with the anti-hCD8 nanobody and an antibody for hCD103. Real-time imaging of these samples revealed that the CD103<sup>-</sup> and CD103<sup>+</sup> epidermal CD8<sup>+</sup> T<sub>RM</sub> cell subsets were intermingled and migrated through the tissue, with comparable speeds (0.54±0.82 and 0.57±0.64  $\mu$ m/min, respectively). In all double positive epidermal T cells, the CD103 antibody complex was enriched at the lagging-end of migrating CD8<sup>+</sup> T<sub>RM</sub> cells (**Fig. 3g** and **Supplementary Video 11**). This location may potentially be explained by labeling-induced receptor clustering, and future studies using different labeling strategies may test this. *Ex vivo* staining of tissue with anti-hCD1a antibody also allowed visualization of Langerhans

cells. MP imaging showed that Langerhans cells were located above CD8<sup>+</sup> skin-resident T<sub>RM</sub> cells in the upper layers of the epidermis pointing their dendritic protrusions upwards (**Fig. 3h**, left image), and with examples of CD8<sup>+</sup> T cells migrating in close proximity (**Fig. 3h**, three right images). In contrast to the motility of CD8<sup>+</sup> T<sub>RM</sub> cells in human epidermis, Langerhans cells remained sessile throughout these recordings (**Supplementary Video 12**).

The majority of human CD8<sup>+</sup> skin-resident T<sub>RM</sub> cells was found to be located in the dermal compartment (**Fig. 3b**), providing the opportunity to also examine migratory behavior of human CD8<sup>+</sup> T<sub>RM</sub> cells at a second tissue site. To this end, real-time MP imaging sessions (3.5-4 h) of skin tissue from 4 individuals were performed. Human CD8<sup>+</sup> skin-resident T<sub>RM</sub> cells migrated through the dermis with median speeds around  $0.40 \pm 1.09 \mu\text{m}/\text{min}$  (**Fig. 4a**, left). Compared to murine epidermal CD8<sup>+</sup> skin-resident T<sub>RM</sub> cells, human dermal CD8<sup>+</sup> T cells showed a larger heterogeneity in speed at the single cell level. Persistence times and motility coefficients were comparable for murine CD8<sup>+</sup> skin-resident T<sub>RM</sub> cells and human dermal T cells when these were estimated from short-term observation windows (**Fig. 4a**, middle and right). However, in contrast to murine CD8<sup>+</sup> skin-resident T<sub>RM</sub> cells, long-term migration of human dermal CD8<sup>+</sup> T cells could not be described as a persistent random walk (**Supplementary Fig. 3d**). Migration of human dermal CD8<sup>+</sup> skin-resident T<sub>RM</sub> cells was observed in both collagen type I-dense and -poor areas (**Fig. 4b**, top image), with a fraction of CD8<sup>+</sup> T cells in collagen type I-poor areas migrating along the perimeter of these structures (**Fig. 4b**, middle and bottom images and **Supplementary Video 13**). Analysis of skin biopsies co-stained with anti-hCD8 nanobody and an antibody for collagen type IV to identify BMs, revealed that these collagen type I-poor regions were frequently filled with dermal vessels such as blood capillaries (**Fig. 4c**, top), and real-time imaging of these explants showed examples of dermal CD8<sup>+</sup> T<sub>RM</sub> cells migrating along the lining of these vessels (**Fig. 4c**, bottom, and **Supplementary Video 14**).

To examine whether local presence of collagen type I affects T<sub>RM</sub> cell migration, we compared speed-steps of T<sub>RM</sub> cells at both sites. While the median speeds for cells in collagen type I-dense or -poor areas was highly similar, fast speed steps were significantly more often observed in collagen type I-poor areas, suggesting that collagen type I forms a barrier for dermal T<sub>RM</sub> cell migration (**Supplementary Fig. 3e**).

Finally, in 3 out of 5 explants analyzed, cases of CD8<sup>+</sup> skin-resident T<sub>RM</sub> cells that migrated in and out of the dermis, as based on the distance from the nearest collagen type I signal, were observed (**Fig. 4d** and **Supplementary Video 15**). While large data sets are required to understand the magnitude of this process, these data suggest that T<sub>RM</sub> cells at the two sites might not be two fully separate compartments.

Collectively, these data demonstrate that human CD8<sup>+</sup> skin-resident T<sub>RM</sub> cells patrol both the epidermal and dermal compartment and, using labeling of 3 cell surface markers and one extracellular protein, show that the *ex vivo* imaging system that we develop here provides a versatile tool to study the behavior of skin-resident immune cell populations in real-time.

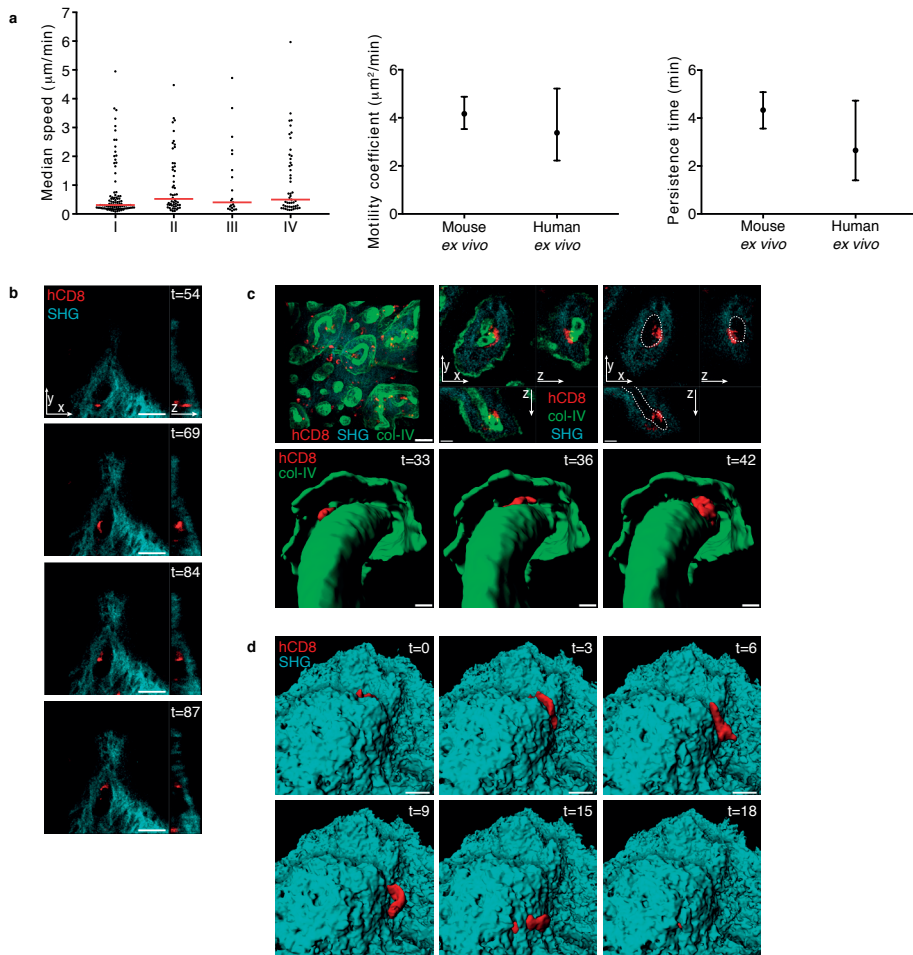


**Figure 4 | Human CD8<sup>+</sup> T<sub>RM</sub> cells patrol the papillary dermis.** **a**, Left: median speeds of individual tracks (black dots) of dermal CD8<sup>+</sup> T<sub>RM</sub> cells of 4 different individuals indicated with I (n=96), II (n=52), III (n=21) and IV (n=49) (3.5-4 h-recordings). Red bar indicates median. Middle and right: estimated motility coefficient (middle) and persistence time (right) with error bars indicating 95% confidence interval (the range  $q_{0.025}$ - $q_{0.975}$ ) based on bootstrapping of the data (black dots indicate median). Murine data is based on n=3 (4 h recordings) and human data on n=4 (3.5-4 h recordings). **b**, Virtual sectioning showing an MP maximum intensity of a hCD8<sup>+</sup> (red) cell migrating along the perimeter of a collagen type I (SHG)-poor area. Scale bars indicate 20  $\mu\text{m}$ . **c**, Top left: Perspective top view of MP recording of anti-hCD8 (red) and anti-collagen type IV (green) stained biopsy (SHG, blue) (scale bar: 50  $\mu\text{m}$ ). Top middle, right: section view of CD8<sup>+</sup> cell located adjacent to a basement membrane positive vessel (scale bar: 15  $\mu\text{m}$ ). Note that collagen type I-poor areas (indicated with dashed white line) are filled with dermal vessels. Bottom: bottom view of 3D surface rendering of hCD8<sup>+</sup> (red) cell migrating along collagen type IV positive (green) dermal vessel (time in minutes). Data are representative of n=3 individuals. **d**, 3D-surface rendering with blend-shading of dermal collagen type I (SHG, blue) and a CD8<sup>+</sup> cell (red) migrating on top of dermal papillae and moving into the dermis around time point t=15 (min). Scale bars indicate 20  $\mu\text{m}$ .

## DISCUSSION

To our knowledge, this is the first longitudinal analysis of the behavior of resident memory T cells in human tissue. To allow this, we established an *ex vivo* imaging system for the *in situ* labeling and real-time tracking of CD8<sup>+</sup> T<sub>RM</sub> cells in human skin. Using this approach, we demonstrate that human CD8<sup>+</sup> cells actively migrate in both the epidermal and dermal layers of the skin, with median speeds in the same range as those of murine CD8<sup>+</sup> skin-resident T<sub>RM</sub> cells. These CD8<sup>+</sup> cells reflect tissue-resident memory T cells, as all CD8<sup>+</sup> cells isolated from both skin compartments express CD69<sup>+</sup>, the principal defining feature of T<sub>RM</sub> cells<sup>6,30</sup>. These data establish that tissue patrol is a property of human CD8<sup>+</sup> skin-resident T<sub>RM</sub> cells, and fit with the model that relatively rare CD8<sup>+</sup> T<sub>RM</sub> cells can act as local sentinels to provide a rapid and tissue-wide anti-pathogen response<sup>20,21</sup>. The observation of T<sub>RM</sub> cell patrol in both the dermis and epidermis, two sites with a different tissue architecture, combined with the notion that tissue patrol has been observed for murine T<sub>RM</sub> cells in multiple organs<sup>16,18,32</sup>, makes it reasonable to postulate that a continuous migratory behavior forms a shared property of all human CD8<sup>+</sup> T<sub>RM</sub> cell populations.

In the epidermal compartment, human CD8<sup>+</sup> T<sub>RM</sub> cells migrate in the stratum basale in a dense environment of keratinocytes. The adhesive interactions between epithelial cells and T lymphocytes includes the binding of E-cadherin to the  $\alpha_E$  (CD103)  $\beta_7$  integrin that is present on many tissue resident T cells<sup>33</sup>. With the caveat that antibody labeling may potentially influence this interaction, in the current dataset we did not find any evidence for a difference in motility between single positive CD8<sup>+</sup> T<sub>RM</sub> cells and those that also express CD103.

Consistent with prior data<sup>34</sup>, the majority of CD8<sup>+</sup> T cells in healthy human skin were observed in the dermal compartment. These cells show a distinct migratory behavior as compared to murine CD8<sup>+</sup> skin-resident T<sub>RM</sub> cells, with a larger heterogeneity in speed. One explanation for this heterogeneity is that the dermis comprises different structures that may form barriers to T<sub>RM</sub> cell migration. Further evidence for a model that local structure may influence T<sub>RM</sub> cell migration parameters comes from the observation that T<sub>RM</sub> cells in dermal areas with a low collagen type I density show a higher frequency of fast steps than those in high-density areas. In line with this, the former areas have been described to contain collagen type III, and connective tissues enriched for this collagen are described to be more flexible compared to collagen type I dense tissues<sup>35,36</sup>. Within areas with low collagen type I density, examples of T<sub>RM</sub> cells migrating along the lining of blood capillaries were observed. Given the strategic positioning of these T<sub>RM</sub> cells, it may be postulated that they are located at these sites to patrol epidermal supply routes. Contrary to the notion of epidermal CD8<sup>+</sup> T<sub>RM</sub> cells as a fully isolated cell compartment that has emerged from mouse model studies, we also encountered examples of human CD8<sup>+</sup> skin-resident T<sub>RM</sub> cells located at the dermal-epidermal junction migrating in and out of the dermis. While the BM forms a tight boundary between

these two compartments, the potential for immune cells to cross this barrier through small pores has previously been suggested by electron microscopy analyses<sup>37</sup>.

From a technological perspective, the successful *ex vivo* staining with anti-CD8 nanobodies, but also with full-size anti-CD1a, anti-collagen type IV and anti-CD103 antibodies, indicates that the current system may be utilized to study a wide variety of skin molecules and cell types of interest in real-time. As in all imaging experiments that use exogenous labels, and as illustrated by the reduction in antigen sensitivity of mouse but not human T cells upon staining with anti-CD8 nanobodies, it will be important to understand whether labeling influences cell behavior. In future studies in healthy human skin it will be interesting to investigate whether the CD4<sup>+</sup> CD103<sup>-</sup> memory T cells that are present at high density in the dermis<sup>29, 30</sup> show a similar patrolling behavior as CD8<sup>+</sup> T<sub>RM</sub> cells, and whether these cells co-localize with either CD8<sup>+</sup> T<sub>RM</sub> cells or defined antigen-presenting cell populations (APCs). Finally, whereas the current study focuses on the behavior of tissue-resident T cells in healthy tissue, this *ex vivo* technology should also provide a tool to study T cell behavior in the effector and memory phase of T<sub>RM</sub> cell-mediated skin conditions<sup>4, 22</sup>.

## REFERENCES

1. Mueller, S.N. & Mackay, L.K. Tissue-resident memory T cells: local specialists in immune defence. *Nat Rev Immunol* **16**, 79-89 (2016).
2. Gebhardt, T., Palendira, U., Tschärke, D.C. & Bedoui, S. Tissue-resident memory T cells in tissue homeostasis, persistent infection, and cancer surveillance. *Immunol Rev* **283**, 54-76 (2018).
3. Thome, J.J. & Farber, D.L. Emerging concepts in tissue-resident T cells: lessons from humans. *Trends Immunol* **36**, 428-435 (2015).
4. Clark, R.A. Resident memory T cells in human health and disease. *Sci Transl Med* **7**, 269rv261 (2015).
5. Mackay, L.K. *et al.* The developmental pathway for CD103(+)CD8+ tissue-resident memory T cells of skin. *Nat Immunol* **14**, 1294-1301 (2013).
6. Sathaliyawala, T. *et al.* Distribution and compartmentalization of human circulating and tissue-resident memory T cell subsets. *Immunity* **38**, 187-197 (2013).
7. Kumar, B.V. *et al.* Human Tissue-Resident Memory T Cells Are Defined by Core Transcriptional and Functional Signatures in Lymphoid and Mucosal Sites. *Cell Rep* **20**, 2921-2934 (2017).
8. Wu, H. *et al.* Pathogenic role of tissue-resident memory T cells in autoimmune diseases. *Autoimmun Rev* **17**, 906-911 (2018).
9. Park, C.O. & Kupper, T.S. The emerging role of resident memory T cells in protective immunity and inflammatory disease. *Nat Med* **21**, 688-697 (2015).
10. Matos, T.R. *et al.* Clinically resolved psoriatic lesions contain psoriasis-specific IL-17-producing alphabeta T cell clones. *J Clin Invest* **127**, 4031-4041 (2017).
11. Edwards, J. *et al.* CD103(+) Tumor-Resident CD8(+) T Cells Are Associated with Improved Survival in Immunotherapy-Naive Melanoma Patients and Expand Significantly During Anti-PD-1 Treatment. *Clin Cancer Res* **24**, 3036-3045 (2018).
12. Webb, J.R., Milne, K., Watson, P., Deleeuw, R.J. & Nelson, B.H. Tumor-infiltrating lymphocytes expressing the tissue resident memory marker CD103 are associated with increased survival in high-grade serous ovarian cancer. *Clin Cancer Res* **20**, 434-444 (2014).
13. Djenidi, F. *et al.* CD8+CD103+ tumor-infiltrating lymphocytes are tumor-specific tissue-resident memory T cells and a prognostic factor for survival in lung cancer patients. *J Immunol* **194**, 3475-3486 (2015).
14. Ganesan, A.P. *et al.* Tissue-resident memory features are linked to the magnitude of cytotoxic T cell responses in human lung cancer. *Nat Immunol* **18**, 940-950 (2017).
15. Duhon, T. *et al.* Co-expression of CD39 and CD103 identifies tumor-reactive CD8 T cells in human solid tumors. *Nat Commun* **9**, 2724 (2018).
16. Ariotti, S. *et al.* Tissue-resident memory CD8+ T cells continuously patrol skin epithelia to quickly recognize local antigen. *Proc Natl Acad Sci U S A* **109**, 19739-19744 (2012).
17. Zaid, A. *et al.* Persistence of skin-resident memory T cells within an epidermal niche. *Proc Natl Acad Sci U S A* **111**, 5307-5312 (2014).
18. Beura, L.K. *et al.* Intravital mucosal imaging of CD8(+) resident memory T cells shows tissue-autonomous recall responses that amplify secondary memory. *Nat Immunol* **19**, 173-182 (2018).
19. Park, S.L. *et al.* Local proliferation maintains a stable pool of tissue-resident memory T cells after antiviral recall responses. *Nat Immunol* **19**, 183-191 (2018).
20. Ariotti, S. *et al.* T cell memory. Skin-resident memory CD8(+) T cells trigger a state of tissue-wide pathogen alert. *Science* **346**, 101-105 (2014).

21. Schenkel, J.M. *et al.* T cell memory. Resident memory CD8 T cells trigger protective innate and adaptive immune responses. *Science* **346**, 98-101 (2014).
22. Cheuk, S. *et al.* CD49a Expression Defines Tissue-Resident CD8(+) T Cells Poised for Cytotoxic Function in Human Skin. *Immunity* **46**, 287-300 (2017).
23. Mort, R.L., Hay, L. & Jackson, I.J. Ex vivo live imaging of melanoblast migration in embryonic mouse skin. *Pigment Cell Melanoma Res* **23**, 299-301 (2010).
24. Masters, B.R. *et al.* Mitigating thermal mechanical damage potential during two-photon dermal imaging. *J Biomed Opt* **9**, 1265-1270 (2004).
25. Li, J.L. *et al.* Intravital multiphoton imaging of immune responses in the mouse ear skin. *Nat Protoc* **7**, 221-234 (2012).
26. Ng, L.G. *et al.* Visualizing the neutrophil response to sterile tissue injury in mouse dermis reveals a three-phase cascade of events. *J Invest Dermatol* **131**, 2058-2068 (2011).
27. Pasparakis, M., Haase, I. & Nestle, F.O. Mechanisms regulating skin immunity and inflammation. *Nat Rev Immunol* **14**, 289-301 (2014).
28. Larsen, C.P. *et al.* Migration and maturation of Langerhans cells in skin transplants and explants. *J Exp Med* **172**, 1483-1493 (1990).
29. Clark, R.A. *et al.* The vast majority of CLA<sup>+</sup> T cells are resident in normal skin. *J Immunol* **176**, 4431-4439 (2006).
30. Watanabe, R. *et al.* Human skin is protected by four functionally and phenotypically discrete populations of resident and recirculating memory T cells. *Sci Transl Med* **7**, 279ra239 (2015).
31. Pozzi, A., Yurchenco, P.D. & Iozzo, R.V. The nature and biology of basement membranes. *Matrix Biol* **57-58**, 1-11 (2017).
32. McNamara, H.A. *et al.* Up-regulation of LFA-1 allows liver-resident memory T cells to patrol and remain in the hepatic sinusoids. *Sci Immunol* **2** <http://dx.doi.org/10.1126/sciimmunol.aaj1996> (2017).
33. Cepek, K.L. *et al.* Adhesion between epithelial cells and T lymphocytes mediated by E-cadherin and the alpha E beta 7 integrin. *Nature* **372**, 190-193 (1994).
34. Cheuk, S. *et al.* Epidermal Th22 and Tc17 cells form a localized disease memory in clinically healed psoriasis. *J Immunol* **192**, 3111-3120 (2014).
35. Shirshin, E.A. *et al.* Two-photon autofluorescence lifetime imaging of human skin papillary dermis in vivo: assessment of blood capillaries and structural proteins localization. *Sci Rep* **7**, 1171 (2017).
36. Omelyanenko, N.P., Slutsky, L.I. & Mironov, S.P. *Connective Tissue: Histophysiology, Biochemistry, Molecular Biology*. Taylor & Francis, 2013.
37. Oakford, M.E. *et al.* Migration of immunocytes across the basement membrane in skin: the role of basement membrane pores. *J Invest Dermatol* **131**, 1950-1953 (2011).

## METHODS

### Mice

C57BL/6j-Ly5.1 (referred to in the text as C57BL/6j mice), C57BL/6j OT-I, C57BL/6j mT/mG, and C57BL/6j UCB-GFP transgenic mice were obtained from Jackson Laboratories, the C57BL/6JRjAlbino strain was obtained from Janvier labs. C57BL/6j gBT I.1 TCR transgenic mice were a kind gift from F. Carbone (Doherty Institute, Australia). All animals were maintained and crossed in the animal department of The Netherlands Cancer Institute (NKI). All animal experiments were approved by the Animal Welfare Committee of the NKI, in accordance with national guidelines.

### Adoptive transfer, DNA vaccination

CD8<sup>+</sup> T cells were obtained from single-cell suspensions of spleens from OT-I-GFP, gBT-GFP, or OT-I-mTmG mice using the mouse CD8<sup>+</sup> T lymphocyte enrichment kit (BD Biosciences). Mice received a total of  $2 \times 10^5$  CD8<sup>+</sup> cells intravenously in the tail vein. DNA vaccination was performed on depilated hind legs of anesthetized mice by application of plasmid DNA encoding TTFC-OVA<sub>257-264</sub> (SIINFEKL), or a mix of TTFC-OVA<sub>257-264</sub> (SIINFEKL) and TTFC-gB<sub>498-505</sub> (SSIEFARL) (3 rounds of vaccination, using 60 µg of DNA per vaccination<sup>38, 39</sup>), by means of a sterile disposable 9-needle bar mounted on a rotary tattoo device (MT.DERM GmbH).

### Generation of fluorescently labeled nanobodies

*Escherichia coli* cells were transformed with the expression vector pHEN6 encoding either the anti-mouse CD8 nanobody 118, or the anti-human CD8 nanobody 218, followed by an LPETGG-6xHis sequence. Bacteria were grown to OD 0.6-0.8 at 37°C and protein production was induced with 1 mM IPTG, overnight at 30°C. Cells were harvested, resuspended in 1x TES buffer (200 mM Tris, pH 8, 0.65 mM EDTA, 0.5 M sucrose) and incubated at 4°C for 1 h. Subsequently, cells were exposed to osmotic shock by 1:4 dilution in 0.25X TES buffer, overnight at 4°C, and the periplasmic fraction was isolated by centrifugation and loaded onto Ni-NTA beads (Qiagen) in 50 mM Tris, pH 8, 150 mM NaCl and 10 mM imidazole. Protein was eluted in 50 mM Tris, pH 8, 150 mM NaCl, 500 mM imidazole, was then loaded onto a Biosep 3000 Phenomenex gel filtration column running in phosphate-buffered saline (PBS), and the appropriate fractions were collected. Purity of recombinant nanobody was assessed by SDS/PAGE analysis, and material was concentrated using an Amicon 10 kDa MWCO filtration unit (Millipore), and stored at -80°C. To generate the fluorescent label, 1 mg of Alexa Fluor-594 (AF594) maleimide dye (Thermo Fisher Scientific) was ligated to 200 µM GGGC peptide in the presence of 10 mM NaHCO<sub>3</sub> and was then purified on a C5 column (Waters). In order to covalently link the fluorescent label to the nanobody, sortase reactions were performed. To this end, purified GGGC-AF594 (80 µM) was incubated with purified

nanobody-LPETGG-6xHis (5  $\mu$ M) and penta- (5M) or hepta- (7M) mutant sortase (0.8  $\mu$ M) for 2 h at 4°C in 50 mM Tris pH 8 and 150 mM NaCl, and in the case of the penta-mutant, 10 mM CaCl<sub>2</sub> was added (sortase was produced in-house according to a previously described protocol using sonification instead of French press<sup>40</sup>). Sortase and unreacted nanobody were removed by adsorption onto Ni-NTA agarose beads (Qiagen). Subsequently, the unbound fraction was added on top of a 100 kDa cut-off filter to remove Ni-NTA agarose beads, flow-through was concentrated, and unconjugated GGGC-AF594 was removed using an Amicon 10 kDa MWCO filtration unit (Millipore) by exchanging the protein solution three times with PBS. The material was further purified using a zeba spin column (Thermo Fisher Scientific). Resulting anti-mouse and anti-human CD8-AF594 nanobody conjugates were stored in aliquots at -20°C. Protein concentrations were determined using nanodrop and individual batches of labeled nanobody were titrated for optimal usage (final concentrations ranging from 5-10  $\mu$ g/ml).

### **Functional analysis of anti-mCD8 nanobody labeled murine T cells *in vitro***

For functional analysis of anti-mCD8 nanobody stained murine T cells *in vitro*, first a spleen of a C57BL/6j OT-I mouse was mashed and resuspended in RPMI (Thermo Fisher Scientific), fetal calf serum (8% final, Sigma-Aldrich), penicillin streptomycin (100 U/ml) and L-glutamine, supplemented with 50  $\mu$ M beta-mercaptoethanol, non-essential amino acids, 1 mM sodium pyruvate and 10 mM HEPES (all Thermo Fisher Scientific) and plated in 96-well tissue-treated plates. Cells were then labeled with anti-mCD8-AF594 or anti-hCD8-AF594 nanobody in the same concentration as used for peptide stimulation experiments in *ex vivo* murine tissue material (5  $\mu$ g/ml final) for 4 h, washed twice, and subsequently stimulated overnight with indicated amounts of OVA<sub>257-264</sub> peptide. After 14-18 h, cells were washed twice and stained with anti-mCD8-beta-PeCy7 (eBioH35-17.2, eBioscience), anti-mouse TCR V beta 5.1/5.2-APC (MR9-4, Thermo Fisher Scientific), anti-mCD25-BV650 (PC61, BioLegend), anti-mCD69-APC-Cy7 (H1.2F3, BioLegend) and 4',6-Diamidino-2-Phenylindole, Dihydrochloride (DAPI) (Sigma-Aldrich) to exclude dead cells, and samples were measured on an LSR II SORP (BD Biosciences). Cells were analyzed according to the gating strategy shown in **Supplementary Fig. 4a**.

### **Functional analysis of anti-hCD8 nanobody labeled human T cells *in vitro***

For functional analysis of anti-hCD8 nanobody stained human T cells *in vitro*, we used T cells transduced with two TCRs that recognize a CDK4-derived neoantigen with different affinities (<sup>41</sup> and unpublished). In brief, T cells were plated in 96-well tissue-treated plates in RPMI (Thermo Fisher Scientific), human serum (8% final, Sigma-Aldrich) and penicillin streptomycin (100 U/ml) (Thermo Fisher Scientific) and labeled with anti-mCD8-AF594 or anti-hCD8-AF594 nanobody in the same concentration as used for *ex vivo* imaging of human tissue material (5  $\mu$ g/ml final) for 4 h. Cells were then washed twice and co-cultured

overnight with JY cells (American Type Culture Collection (ATCC) loaded with the indicated concentrations of CDK4<sub>mut</sub> peptide (ALDPHSGHFV<sup>41</sup>), or with the CDK4<sub>wt</sub> cell line MM90904 (a kind gift from M. Donia, Herlev Hospital, Denmark) or the CDK4<sub>mut</sub> cell line NKIRTL006<sup>42</sup> at a 1:1 ratio. After 14–18 h incubation, cells were washed twice and stained with anti-hCD8a-PerCP-Cy5.5 (SK1, BioLegend), anti-mouse TCR beta-AF488 (H57-597, BioLegend) to detect the TCR-modified cells<sup>41</sup>, anti-hCD137-BV421 (4B4-1, BioLegend) and IR-dye (Thermo Fisher Scientific) to exclude dead cells, and samples were measured on an LSR II SORP (BD Biosciences). Cells were analyzed according to the gating strategy shown in **Supplementary Fig. 4b**.

### **Ex vivo preparation, ex vivo labeling, and ex vivo peptide stimulation of mouse tissue**

Skin tissue of depilated hind legs of sacrificed mice was obtained using forceps and cleared of connective tissue and fat. Skin pieces were mounted in *ex vivo* Lumox 35-mm dishes (for adherent cells, Sarstedt), with the epidermis facing downwards to the gas-permeable bottom. For analysis of a non-air exposed setup, a 35-mm glass-bottom Willco dish was utilized (WillCo wells). A gas-permeable film (8  $\mu$ m pores, 25-mm diameter, Sigma-Aldrich) was placed on top of the dermal side of the skin, followed by a layer of LDEV-Free reduced growth factor basement membrane matrix matrigel (Geltrex, Invitrogen) and culture medium consisting of Opti-MEM (Thermo Fisher Scientific), fetal calf serum (8% final, Sigma-Aldrich), penicillin streptomycin (100 U/ml) and L-glutamine (both Thermo Fisher Scientific). When imaging *ex vivo* tissue directly after harvest and mounting, skin-resident T<sub>RM</sub> cells exhibited a higher circularity and were relatively immobile, but cells regained motility and dendricity overnight (data not shown). Histopathological analysis showed that skin conditions deteriorate over time, with mild alterations in the first 24 h but signs of severe skin degeneration apparent at 72 h (**Supplementary Fig. 2d**, top). For these reasons, all *ex vivo* experiments were performed after an overnight recovery period, but no later than 24 h after mounting. For *ex vivo* labeling, skin samples were incubated with anti-mouse or anti-human CD8-AF594 nanobodies overnight at 37°C and 5% CO<sub>2</sub> and washed 2 times before imaging. For peptide stimulations, OVA<sub>257–264</sub> peptide was added to the *ex vivo* culture medium (80 nM final concentration) and imaging was performed immediately thereafter.

### **In vivo and ex vivo mouse skin imaging**

Isflurane anesthetized mice with depilated areas of the hind legs were placed in a custom-built chamber with the skin placed against a coverslip at the bottom side of the chamber. In case of imaging of *ex vivo* skin tissue, the dish with mounted tissue was placed in an inlay, with the epidermal side facing downwards. The lid of the dish was removed and the dish was covered with gas permeable CultFoil to prevent evaporation (Pecon), topped by a custom-built cover connected to a CO<sub>2</sub>-flow. Images were acquired using an inverted Leica TCS

SP5 confocal scanning microscope equipped with diode and Argon lasers and enclosed in a custom-built environmental chamber that was maintained at 37°C using heated air. Images were acquired using a 20×/0.7 N.A. dry objective. GFP was excited at 488 nm wavelength and collected between 498-550 nm. To visualize AF594 signal, the sample was excited at 594 nm and signal was detected between 604-700 nm. For imaging of mTmG<sup>+</sup> cells, 561 nm was used to excite tissue and signal was collected at 571-700 nm. Three-dimensional z-stacks (typical size 388 μm × 388 μm × 23 μm; typical voxel size 0.8 μm × 0.8 μm × 1.0 μm) were captured every 2 min for a period of up to 4 h.

## Histopathology and immunohistochemistry

For histopathological analyses, 2 μm thick formalin-fixed, paraffin-embedded full-thickness murine tissue slides were stained with hematoxylin-eosin. Immunohistochemical analysis was performed on 4 μm thick serially cut slides stained with anti-GFP (ab6556, Abcam) or anti-Langerin (CD207, eBioRMUL.2, eBioscience) antibodies. Antibody staining was revealed with 3,3'-diaminobenzidine (Sigma). Slides were evaluated and scored by an animal pathologist blinded to experimental conditions.

## Ex vivo imaging of human skin

Punch biopsies (5 mm) were taken from resected normal human skin tissue directly after abdominoplastic- or breast reconstructing surgery, obtained in accordance with national ethical guidelines. Skin was cleared of fat and connective tissue and mounted as described in **Fig. 1a**. For *ex vivo* labeling, samples were incubated with anti-mouse or anti-human CD8-AF594 nanobody, Hoechst 33342 (5-10 μg/ml final concentration, Thermo Fisher Scientific), anti-human-CD1a-AF488 antibody (4-8 μg/ml final concentration, HI149, BioLegend), anti-human-collagen type IV-AF488 antibody (6.25-12.5 μg/ml final concentration, 1042, Thermo Fisher Scientific) or anti-human-CD103-AF488 (concentrated on a 100 kDa cut-off Amicon spin column (Millipore) and resuspended in PBS to remove sodium azide, used in 5-10 μg/ml final, Ber-ACT8, BioLegend) overnight at 37°C and 5% CO<sub>2</sub>, as indicated. Antibodies were titrated per individual, to accommodate variability in skin thickness and permeability. For subsequent multiphoton (MP) imaging, *ex vivo* culture dishes were washed 2 times and topped with *ex vivo* culture medium (as described in 'Ex vivo preparation, ex vivo labeling, and ex vivo peptide stimulation of mouse tissue' of the 'Materials and Methods'-section), enclosed with parafilm and placed under an upright Leica SP8 system equipped with a Spectraphysics Insight Deepsee laser. Images were acquired with a 25×/0.95 N.A. water immersion objective (Leica Fluotar VISIR), two NDD HyD detectors and an 8,000-Hz resonant scanner in a custom-built environmental chamber that was maintained at 37°C using heated air supplemented with 5% CO<sub>2</sub>. For detection of AF594 and AF488, wavelength was tuned to 800 nm and collected at a 615/30 and 525/50 band pass filters (bp), respectively. For detection of the second harmonics signal (SHG), wavelength was tuned to 1050 nm and

collected at 525/50bp. For detection of Hoechst signal, laser was tuned to 800 nm and collected at 450/65bp. Three-dimensional stacks (typical size 591  $\mu\text{m}$   $\times$  591  $\mu\text{m}$   $\times$  130  $\mu\text{m}$ ; typical voxel size 0.6  $\mu\text{m}$   $\times$  0.6  $\mu\text{m}$   $\times$  1.0  $\mu\text{m}$ ) were captured every 3 min for periods of up to 4 h. For identification of basement membrane-positive structures as blood capillaries, anti-collagen type IV staining was scored by two independent pathologists. Provided that the human skin sample was imaged within the pre-determined 24 h time window and stained with optimally titrated antibodies, motile CD8<sup>+</sup> T cells could be observed in all samples (n=18 donors), with cells having a large heterogeneity in cell speed. Note that Hoechst dye must be titrated carefully, as excess amounts reduce CD8<sup>+</sup> T cell mobility.

### **Flow cytometry of human skin samples**

For analysis of human skin-resident T<sub>RM</sub> cells by flow cytometry, fresh full-thickness human skin was kept at 4°C overnight and 0.4 mm sheets were prepared by a dermatome the next morning. Subsequently, epidermis and dermis were separated after a 2 h incubation with dispase (0.2% wt/vol, Sigma-Aldrich) at 37°C. Epidermis was further digested using Trypsin-EDTA (0.05% final, Thermo Fisher Scientific), for 30 min at 37°C. Single-cell suspensions of the dermis were obtained by incubation with collagenase type I (0.2% final, Invitrogen) and DNase (30 IU/ml, Sigma) under continuous agitation for 2 h at 37°C. Single cell suspensions were cultured overnight in low-dose human recombinant-IL-2 (30 IU/ml, Novartis) in RPMI (Thermo Fisher Scientific), fetal calf serum (8% final, Sigma-Aldrich), penicillin streptomycin (100 U/ml) and L-glutamine (both Thermo Fisher Scientific). Cells were subsequently stained with anti-CD8-BB700 (HIT8a, BD Biosciences), anti-CD69-BV421 (FN50, BioLegend), and anti-CD103-PE (Ber-ACT8, BioLegend). Single cell suspensions of MP-imaged biopsies were counterstained with anti-CD8-PerCP-Cy5.5 (SK1, BioLegend). Dead cells were excluded using near-IR-dye (Thermo Fisher Scientific). Flow cytometry data were acquired using an LSR II SORP (BD Biosciences). Cells were analyzed according to the gating strategy shown in **Supplementary Fig. 4c**.

### **Data analysis**

For image analysis, raw data (murine recordings) or Gaussian filtered data (automatically determined radius, human recordings) was processed with Imaris (Bitplane). To improve visualization of objects located deep in human skin tissues, an attenuation correction was performed, as determined by a correction factor measured on the AF594 channel intensity in 'slice' viewer. In order to track fluorescent objects, the Imaris Spots module was used to calculate cell coordinates (mean positions) over time. In the subsequent analyses, performed in R (freely available at [www.r-project.org](http://www.r-project.org)) and in Perl (freely available at [www.perl.org](http://www.perl.org)), cellular mean positions within a 10  $\mu\text{m}$  distance from the lateral image borders were discarded, as these would slightly bias the results (e.g., underestimate the speeds)<sup>43</sup>. Tissue drift was corrected by tracking mean positions of stationary reference points resulting from

autofluorescence and/or second harmonics signal and by using the shift in these stationary points to correct the cellular movement. For the analysis to determine the effect of prior imaging time on speed, 2D speeds were calculated based on cell coordinates in a step-based manner<sup>43</sup>, i.e., migration steps were treated independent of the track they originated from. The large majority of recordings (>91.3%) showed a T<sub>RM</sub> cell migration speed that was approximately stable over time; in one case a gradual decrease and in one case a decay in speed at later time points was observed, likely indicative of a general decrease in cell viability in these samples. For this reason, the data from the time frames with a decay in speed were not utilized. To determine migration on a per cell basis, 2D speeds were calculated based on cell coordinates and medians were calculated per cell. Turning angles between consecutive movement steps were determined by calculating the angle between vectors representing these steps, and medians were calculated per cell. For both speeds and turning angles on a per cell basis only tracks with a minimum of 5 time points were incorporated. Motility coefficients and persistence times were estimated from mean square displacement (MSD) plots by fitting Fürth's equation<sup>44</sup> for a persistent random walk, i.e.,  $x^2 = 2nM(t - P_t(1 - e^{-t/P_t}))$ , where  $x^2$  is the mean square displacement,  $n$  is the dimension of the space,  $M$  is the motility coefficient,  $P_t$  is the persistence time, and  $t$  is the elapsed time period since the start of the trajectory. To quantify the average motility behavior across multiple replicates, a 95% confidence interval (CI) was calculated based on bootstrapping of tracks from actually observed tracks. To this purpose, artificial instances of replicates were generated by first randomly selecting the same number of tracks from a replicate as in the original replicates (with replacement). Subsequently, a weighted average of these tracks was determined, where the weight was based on the number of intervals occurring within each track. For instance, a track that is observed during 10 subsequent time points contributes 4 times to the observation of a time window of length 5, whereas a track observed during 14 subsequent time points contributes 8 times to this time window, thus the latter obtains a 2-fold higher weight in the calculation. The 95% CI for  $M$  and  $P_t$  was determined based on 1,000 instances of such artificially generated replicates. In order to compare motility parameters of human versus mouse skin-resident T<sub>RM</sub> cells, we fitted the data on the first 15 min of the MSD because the human migration data do not conform to the pattern expected for persistent random walkers on long time intervals.

To investigate the relationship between local collagen type I (SHG) signal and dermal CD8<sup>+</sup> T<sub>RM</sub> cell speed, a 3D-surface was created on SHG signal (Gaussian smoothing factor, filter width: 0.75  $\mu$ m) and segmented into a binary signal (Imaris). Step-based speeds were then calculated for the tracks based on their 3D distance to the nearest SHG-positive voxel, i.e., steps starting at a maximum distance of 1  $\mu$ m from an SHG voxel were classified as being inside collagen type I ('SHG<sup>+</sup>') and those at a larger distance as being outside collagen type I ('SHG<sup>-</sup>'). Distributions of artificial replicates were generated by randomly sampling an equal number of observations from the SHG<sup>+</sup> and SHG<sup>-</sup> steps, as in the original data (with

replacement). The 95% CI for the 0.75 quantile was determined based on 1,000 replicate instances.

For visual clarity of the MP maximal projections in **Fig. 3a** and **Supplementary Video 8 and 11**, the autofluorescent layer at the top of the epidermal side (observed in all samples in all channels) was removed using the 'surfaces' and 'mask' functions in Imaris. To reduce noise in the overview images in **Fig. 3a** and **Fig. 3g** and **Supplementary Video 11**, a median filter was applied (1-pixel radius). Bleed through of AF488 into the SHG and AF594 channel was corrected in **Supplementary Video 14-I and 15-III** by a spillover-factor determined by intensity measurements in the Imaris 'slice viewer'. For the quantification of human CD8<sup>+</sup> T cells in the epidermal and dermal skin compartments, the position of AF594<sup>+</sup> objects relative to collagen type I (SHG) was determined in the 'section-' and 'slice viewer', where cells located above the SHG signal were categorized as epidermal, whereas cells located below the start of the SHG signal were allocated to the dermal compartment. Human dermal CD8<sup>+</sup> skin-resident T<sub>RM</sub> cells were defined as tracks located below the start of the SHG signal for the entire duration of the recording.

Circularity of GFP<sup>+</sup> murine skin-resident T<sub>RM</sub> cells was assessed using an in-house developed macro in Fiji<sup>45</sup>. In short, recordings were first filtered by a 3D median filter (0.5-pixels radius) to reduce noise, after which maximum intensity projections were created. Cells were then segmented using automatic thresholding (RenyiEntropy) for each frame. Circularity is measured as  $4pA/P^2$  (where A is the projected (2D) cell area and P is the 1D cell perimeter).

For flow cytometry experiments, data was analyzed using FlowJo (Tree Star). Graphs were made in GraphPad Prism (GraphPad Software) or in R.

### **Code availability**

The custom developed macro for measuring circularity of fluorescent cells is publicly available at [https://github.com/bvandenbroek/NKI\\_ImageJ\\_Macros/tree/master/Measure\\_cell\\_circularity](https://github.com/bvandenbroek/NKI_ImageJ_Macros/tree/master/Measure_cell_circularity).

### **Statistics**

Statistical analyses were performed in Prism (GraphPad), two-tailed Mann-Whitney U-tests were used with results being regarded as statistically significant at a P-value of <0.05.

### **Data availability**

Publicly available source data were not used in this study. Data supporting the findings of this study are available from the corresponding author upon reasonable request. **Supplementary Video 1-15** are available via the following link: <https://www.nature.com/articles/s41590-019-0404-3#Sec23>.

## REFERENCES METHODS

38. Bins, A.D. et al. A rapid and potent DNA vaccination strategy defined by in vivo monitoring of antigen expression. *Nat Med* 11, 899-904 (2005).
39. Oosterhuis, K., Aleyd, E., Vrijland, K., Schumacher, T.N. & Haanen, J.B. Rational design of DNA vaccines for the induction of human papillomavirus type 16 E6- and E7-specific cytotoxic T-cell responses. *Hum Gene Ther* 23, 1301-1312 (2012).
40. Antos, J.M. et al. Site-Specific Protein Labeling via Sortase-Mediated Transpeptidation. *Curr Protoc Protein Sci* 89, 15.3.1-15.3.19 (2017).
41. Stronen, E. et al. Targeting of cancer neoantigens with donor-derived T cell receptor repertoires. *Science* 352, 1337-1341 (2016).
42. Kvistborg, P. et al. Anti-CTLA-4 therapy broadens the melanoma-reactive CD8<sup>+</sup> T cell response. *Sci Transl Med* 6, 254ra128 (2014).
43. Beltman, J.B., Maree, A.F. & de Boer, R.J. Analysing immune cell migration. *Nat Rev Immunol* 9, 789-798 (2009).
44. Fürth, v.R. Die Brownsche Bewegung bei Berücksichtigung einer Persistenz der Bewegungsrichtung. Mit Anwendungen auf die Bewegung lebender Infusorien. [Brownian motion under consideration of a persistence of the direction of movement. With applications to the movement of living Infusoria.] *Z Phys* 2, 244-256 (1920).
45. Schindelin, J. et al. Fiji: an open-source platform for biological-image analysis. *Nat Methods* 9, 676-682 (2012).

## Acknowledgements

Plasmid sequences for anti-mouse and anti-human CD8 nanobodies were kindly provided by 121Bio, LLC, with support of M. Gostissa and G. Grotenbreg (Agenus Inc. subsequently acquired substantially all the assets of 121Bio, LLC). We thank H. Ploegh (Harvard, USA) for providing the sortase expression vector and D. Elatmioui and H. Ovaa (LUMC, The Netherlands) for the GGGC-peptide. We would like to acknowledge P.G.L. Koolen (Rode Kruis Ziekenhuis), T. Venema (Slotervaart ziekenhuis) and W.G. van Selms (Onze Lieve Vrouwe Gasthuis – west) and staff of the Plastic Surgery departments for providing human skin tissue. We thank M. Hoekstra for illustrations, M. Willemsen, L. Brocks, L. Oomen, T. Rademakers, the NKI flow cytometry and animal facility for technical support, and S. Ariotti and members of the Schumacher and Haanen laboratories for discussions. This work was supported by an EADV Research Fellowship (to T.R.M.), and ERC AdG Life-His-T (to T.N.S.).

## Author information

Tiago R Matos and Mark Hoogenboezem contributed equally to this work.

## Contributions

F.E.D. performed experiments and analyzed data. M.H. performed multiphoton imaging, J.B.B. analyzed migration parameters. M.T. produced fluorescently labeled nanobodies and performed *in vitro* T cell activation experiments. F.E.D., M.M. and B.vdB. designed imaging analysis. J.-Y.S. evaluated IHC data. T.R.M. and M.B.M.T. organized human skin

material. F.E.D., T.R.M., M.H., M.T., D.W.V., M.B.M.T., R.M.L., J.B.B. and T.N.S. contributed to experimental design. F.E.D., J.B.B. and T.N.S. prepared the manuscript with input of all co-authors.

### **Competing interests**

The authors declare no competing financial interests.

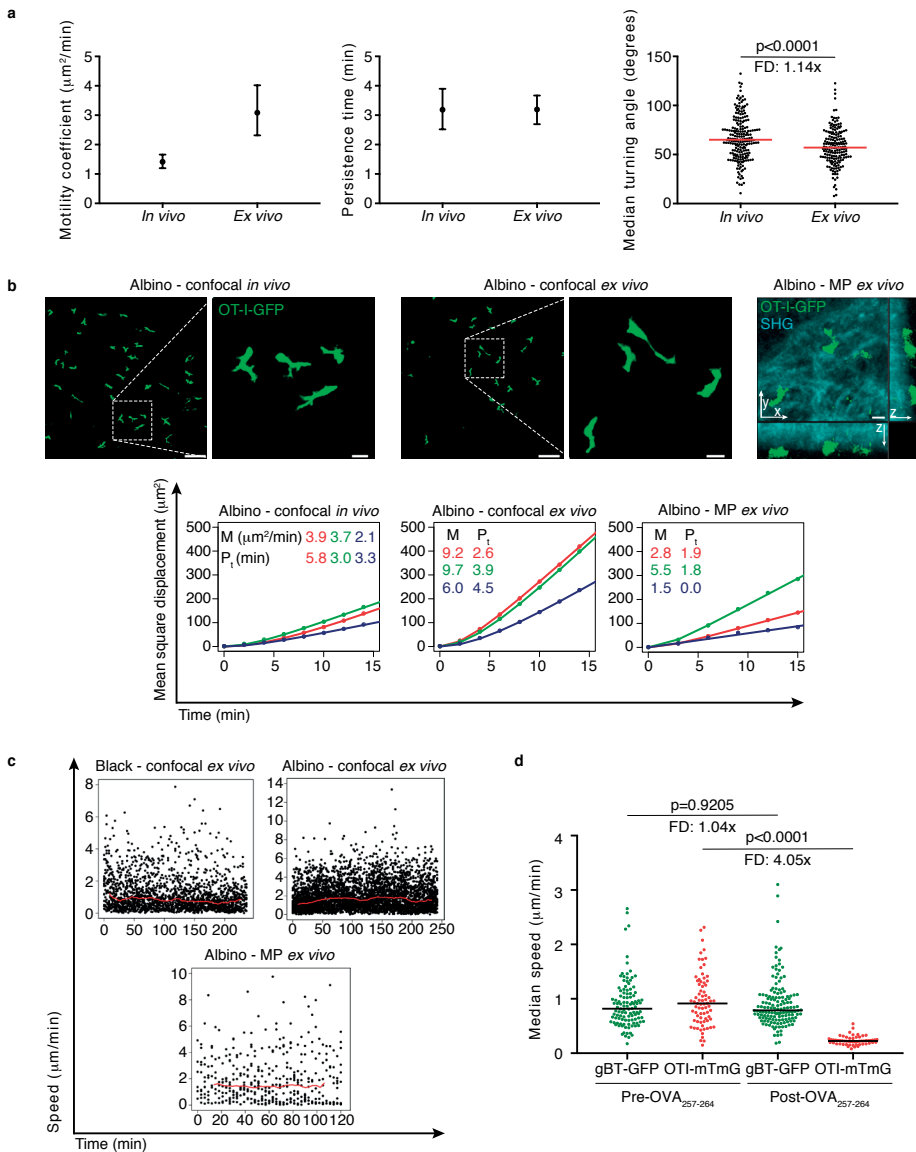
### **Corresponding authors**

Correspondence to Ton N. Schumacher.

**SUPPLEMENTARY INFORMATION**

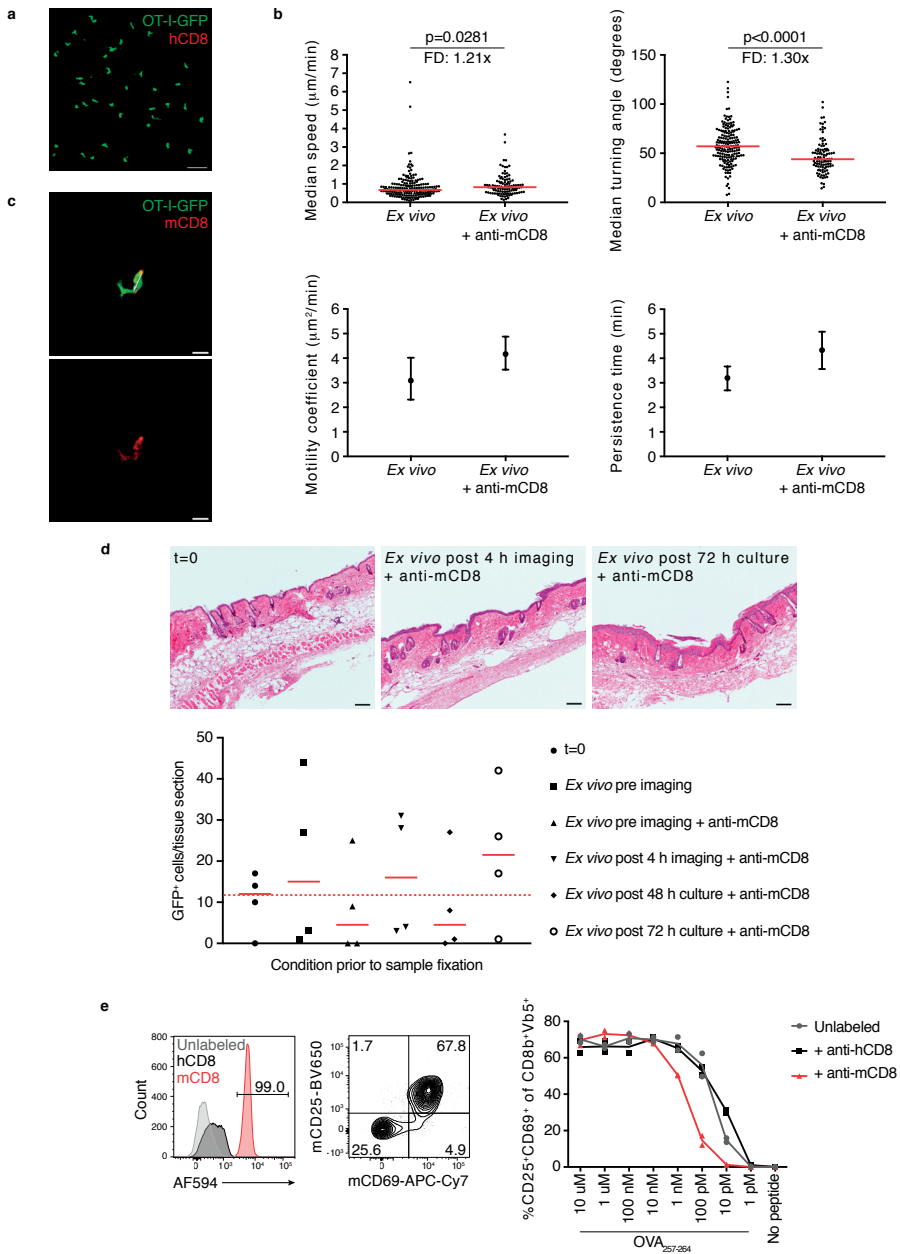
**Supplementary Table 1 | Langerhans cells in *ex vivo* murine tissue.** Semi-quantitative analysis of CD207 (Langerin) staining of murine tissue harvested at indicated conditions. '+': positive; '-/+': some negative areas mixed with positive areas.

	t=0	<i>ex vivo</i> pre imaging	<i>ex vivo</i> pre imaging +anti-mCD8	<i>ex vivo</i> post 4h imaging + anti-mCD8	<i>ex vivo</i> post 4h culture + anti-mCD8	<i>ex vivo</i> post 72h culture + anti-mCD8
<b>mouse 1</b>	+	-/+	-/+	+	+	-/+
<b>mouse 2</b>	+	-/+	+	+	+	-/+
<b>mouse 3</b>	+	+	+	-/+	-/+	-/+
<b>mouse 4</b>	+	+	+	-/+	+	+



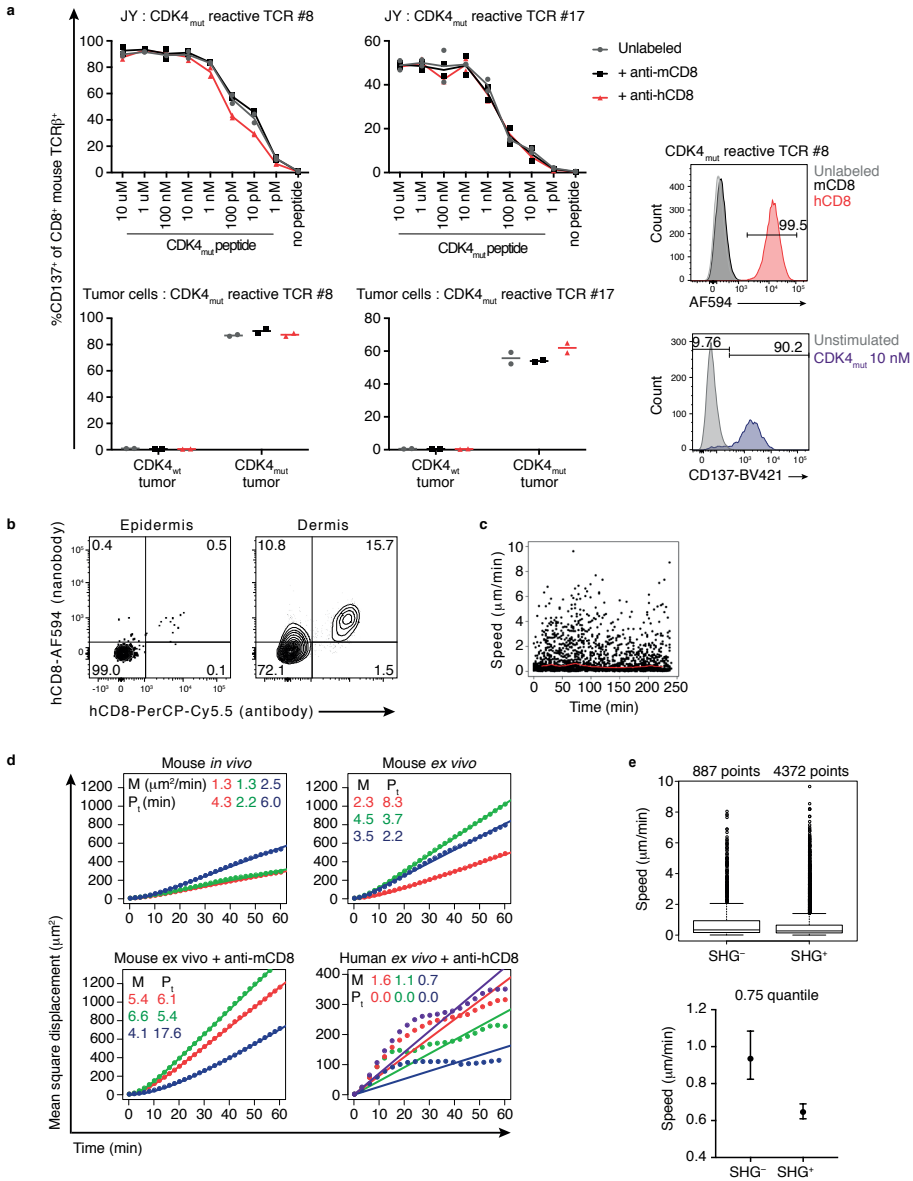
**Supplementary Figure 1 | Validation of *ex vivo* imaging technology.** **a**, Estimated motility coefficient (left) and estimated persistence time (middle), with error bars indicating 95% confidence interval (the range  $q_{0.025}$ - $q_{0.975}$ ) based on bootstrapping of the data for *in vivo* ( $n = 3$  mice) and *ex vivo* ( $n = 3$  mice) murine skin-resident  $T_{RM}$  cells (black dots represent median). Right: black dots indicate median turning angles of individual tracks for *in vivo* ( $n = 208$ ) and *ex vivo* ( $n = 177$ ) murine skin-resident  $T_{RM}$  cells ( $n = 3$  mice each), with red lines indicating medians of all tracks. **b**, Top: confocal maximum intensity projections of OT-I-GFP  $T_{RM}$  cells in skin of C57BL/6 albino mice recorded *in vivo* (left) or *ex vivo* (middle) and multiphoton (MP) section view of OT-I-GFP  $T_{RM}$  cells in skin of C57BL/6 albino mouse recorded *ex vivo* (right; SHG, blue). Images are representative of  $n = 3$  mice per condition. Scale bars indicate  $50 \mu\text{m}$  and  $10 \mu\text{m}$  for overviews and zoomed images, respectively. Bottom: plots of mean square displacement

( $\mu\text{m}^2$ ) versus time (min) using a 15 min time window to estimate motility coefficient (M) and persistence time (Pt) (individual mice are shown in different colors, dots represent data points and lines the best fits). Data are based on 1-4 h recordings, n=3 mice. **c**, Speeds of individual movement steps over time (black dots) of representative confocal (top) or MP (bottom) imaging of *ex vivo* OT-I-GFP T<sub>RM</sub> cells in skin of C57BL/6 black (left) or albino mice (right). Red line indicates running average of 10 movement steps. **d**, Median speed of individual tracks of gBT-GFP (green dots, pre: n=110, post: n=146) and OT-I-mTmG (red dots, pre: n=75, post: n=56) *ex vivo* skin-resident T<sub>RM</sub> cells before and after OVA<sub>257-264</sub> peptide addition. Black line indicates median of all tracks. Data is based on n=3 mice, based on 1-2 h recordings. In **a** and **d**, the statistical test performed is a two-tailed Mann-Whitney U-test, and FD indicates fold difference.



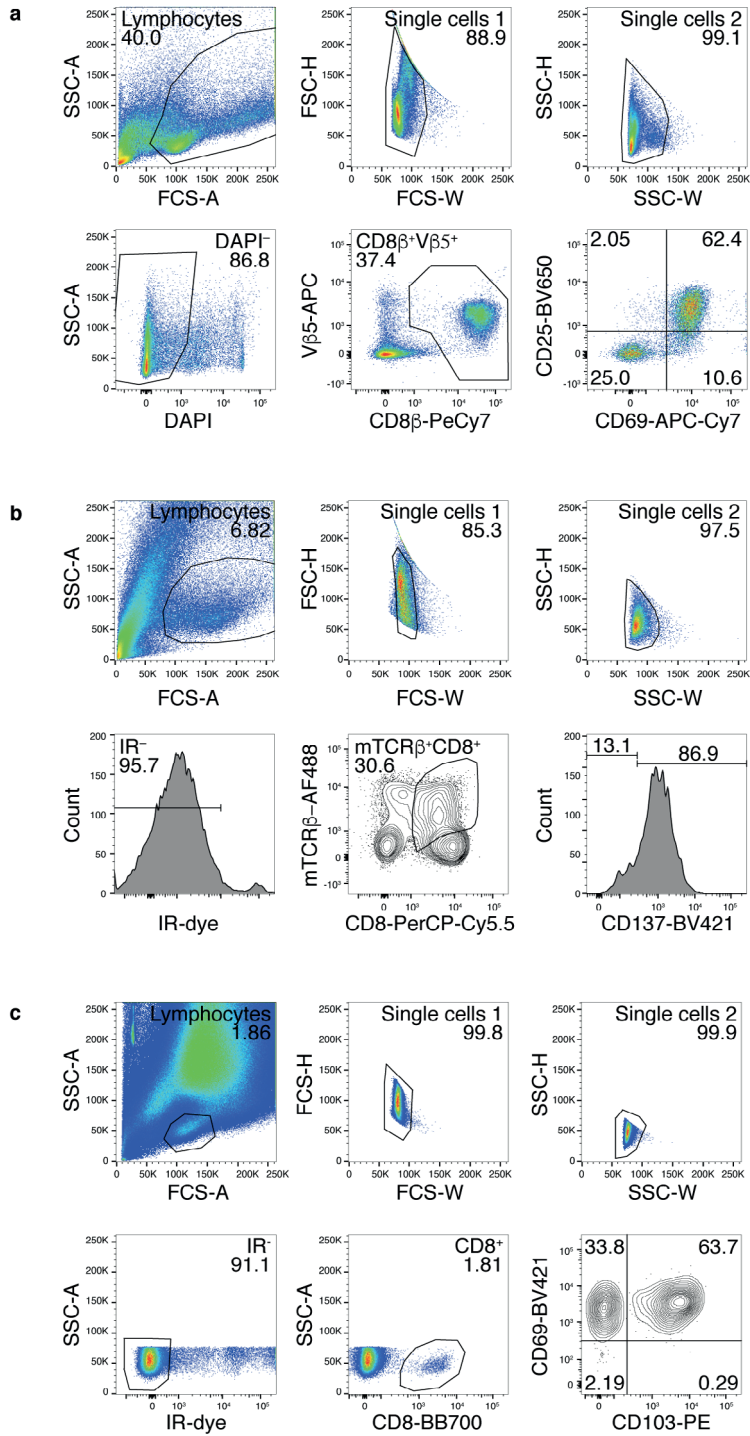
**Supplementary Figure 2 | Validation of anti-mCD8 nanobody labeling of *ex vivo* murine skin-resident  $T_{RM}$  cells.** **a**, Confocal maximum intensity projection of OT-I-GFP (green) T cells stained with anti-hCD8-AF594 (red) nanobody. Scale bar indicates 50  $\mu\text{m}$ . Representative of  $n=2$  mice. **b**, Top: *ex vivo* (left, median speed,  $n=185$ ; right, turning angle,  $n=177$ ) and *ex vivo* nanobody labeled (left, median speed,  $n=107$ ; right, turning angle,  $n=102$ ) skin-resident  $T_{RM}$  cells. Black dots represent individual tracks, red lines indicate median of cell population. Statistical differences were determined using a

two-tailed Mann-Whitney U-test. FD indicates fold difference. Bottom: estimated motility coefficient (left) and persistence time (right) for *ex vivo* and *ex vivo* nanobody labeled skin-resident T<sub>RM</sub> cells. Error bars indicate 95% confidence interval (the range  $q_{0.025}$ - $q_{0.975}$ ) based on bootstrapping of the data (dots represent median) (n=3 mice, 4 h-recordings). **c**, Representative confocal maximum projection of OT-I-GFP T<sub>RM</sub> cells (green) stained with anti-mCD8-AF594 (red). White arrow indicates direction of movement of cell for 6 migration steps. Note that AF594 signal is enriched at the rear side of the cell. Scale bar indicates 10  $\mu$ m, based on n=3 mice. **d**, Top: H&E staining of murine tissue fixed either directly after harvest (t=0, left), after *ex vivo* nanobody labeling and a 4 h-confocal imaging session performed within 24 h after mounting (middle), or after *ex vivo* nanobody labeling and *ex vivo* culture for 72 h (right). Scale bar indicates 100  $\mu$ m. Representative of n=4 mice per condition. Bottom: enumeration of GFP<sup>+</sup> cells by IHC of tissue fixed after indicated treatments. Symbols represent individual mice, solid red line indicates median, dashed red line indicates median at t=0, n=4 mice. **e**, Left: histogram of unstimulated OT-I cells showing specific staining of the anti-mCD8-AF594 nanobody. Cells are gated on single/live/CD8 $\beta$  lymphocytes. Middle: exemplary flow cytometry plot of T cells stimulated with 10 nM OVA257-264 peptide. Right: Percentage of CD25<sup>+</sup>CD69<sup>+</sup> cells of unlabeled (grey), anti-hCD8-AF594 (black) or anti-mCD8-AF594 (red) labeled T cells upon *in vitro* overnight stimulation with indicated amounts of OVA<sub>257-264</sub> peptide. Cells are gated on single/live/CD8 $\beta$ <sup>+</sup>V $\beta$ 5<sup>+</sup> lymphocytes. Symbols indicate technical replicates, lines connect means. Data are representative of 2 experiments.



**Supplementary Figure 3 | Validation of anti-hCD8 nanobody labeling of *ex vivo* human skin-resident  $T_{RM}$  cells.** **a**, Four left plots: percentage of CD137<sup>+</sup> cells of unlabeled (grey), a-mCD8-AF594 labeled (black) or a-hCD8-AF594 (red) labeled TCR-transduced CD8<sup>+</sup> T cells (clone #8, left; clone #17, right) in response to *in vitro* overnight stimulation with indicated peptide-loaded cells. Symbols indicate technical replicates, lines connect means. Top right: histogram of unstimulated cells showing specific staining of the a-hCD8-AF594 nanobody. Cells are gated on single/live/CD8<sup>+</sup> lymphocytes. Bottom right: exemplary histogram of CD137<sup>+</sup> T cells stimulated with 10 nM CDK4<sub>mut</sub> peptide. Cells are gated on single/live/CD8<sup>+</sup>mTCR $\beta$ <sup>+</sup> lymphocytes. Data of clone #8 is representative of 1 and clone #17 of 2 experiments. **b**, Representative flow cytometry plot (of n=2 individuals) of *ex vivo* human tissue stained *in situ*

with anti-hCD8 nanobody that was subsequently digested into single cell suspensions of epidermis and dermis, and then stained with anti-hCD8 antibody. Cells are gated on single/live lymphocytes. **c.** Speeds of individual movement steps during a representative 4 h recording of human *ex vivo* skin-resident T<sub>RM</sub> cells (red line indicates the running average of 10 movement steps). **d.** Mean square displacement ( $\mu\text{m}^2$ ) versus time (min) plot using a 60 min time window to estimate motility coefficient (M) and persistence time (Pt) of the indicated conditions (individual replicates are shown in different colors, dots represent data points and lines the best fits) (based on 3.5-4 h recordings). **e.** Top: box and whiskers (representing 1.5 times the interquartile range) plot showing distribution of speed-steps of dermal CD8<sup>+</sup> T<sub>RM</sub> cells in collagen type I-poor ('SHG<sup>-</sup>', n=887) or -rich ('SHG<sup>+</sup>', n=4372) areas (n=4 individuals). Low and high ends of the box represent the 0.25 ( $q_{0.25}$ ; i.e., the speed where 25% of observations lies below and 75% of observations above) and 0.75 ( $q_{0.75}$ ) quantile and the line in between represents the median; lower whisker represents  $q_{0.25}-1.5*\text{IQR}$  (interquartile range) and upper whisker  $q_{0.75}+1.5*\text{IQR}$ ; black dots represent outliers. Note that the distribution of the SHG<sup>-</sup> speed-steps is more skewed than that of the SHG<sup>+</sup> steps (e.g.,  $q_{0.75}$  is higher in the SHG<sup>-</sup> group). Bottom: estimated 95% confidence interval (CI) for  $q_{0.75}$  based on bootstrapping of the data (n=4 individuals), showing that the speed distributions of SHG<sup>-</sup> and SHG<sup>+</sup> groups are different, as indicated by nonoverlapping CIs. Dots represent medians of all bootstrapped  $q_{0.75}$  values and error bars represent 95% CIs (the range  $q_{0.025}-q_{0.975}$ ). 95% CIs for 0.25 and 0.5 quantiles were also determined and resulted in smaller differences between CIs of SHG<sup>-</sup> and SHG<sup>+</sup> (data not shown).



**Supplementary Figure 4 | Gating strategies of murine and human T cells.** **a.** Analysis of in vitro stimulated murine T cells. Panel shows a sample of unlabeled OT-I splenocytes after overnight culture with 100 pM OVA<sub>257-264</sub> peptide. Lymphocyte population was selected by FSC-A/SSC-A gating. Doublets were then gated out by FSC-A/FSC-H and additional gating on SSC-A/SSC-H. Dead cells were excluded by gating on DAPI<sup>-</sup> cells. CD8<sup>+</sup> OT-I T cells were then gated out on CD8 $\beta$  and V $\beta$ 5 positivity. Subsequently, reactive T cells were gated out by selecting CD25 and CD69 double positive cells (quantification plotted in Supplementary Fig. 2e) (representative of 2 experiments). **b.** Analysis of in vitro stimulated human T cells. Panel shows a sample of unlabeled CDK4<sub>mut</sub> reactive TCR clone #8 T cells after overnight coculture with 10 nM CDK4mut-peptide loaded JI cells. Lymphocyte population was selected by FSC-A/SSC-A gating. Doublets were then gated out by FSC-A/FSC-H and additional gating on SSC-A/SSC-H. Dead cells were excluded by gating on IR<sup>-</sup> cells. TCR modified cells were then gated out based on mTCR $\beta$  and CD8 positivity. Subsequently, reactive cells were selected by positivity for CD137 (quantification plotted in Supplementary Fig. 3a) (representative of 1 experiment). **c.** Analysis of human CD8<sup>+</sup> skin-resident T<sub>RM</sub> cells. Panel shows a single cell suspension of the epidermis. Lymphocyte population was selected by FSC-A/SSC-A gating. Doublets were then gated out by FSC-A/FSC-H and additional gating on SSC-A/SSC-H. Dead cells were excluded by gating on IR<sup>-</sup> cells. Cells were subsequently gated on CD8, followed by CD69 versus CD103 (quantification plotted in Fig. 3c) (representative of n=3 individuals).

## Supplementary Videos

**Supplementary Video 1 | Murine skin-resident  $T_{RM}$  cell migration *in vivo*.** Confocal maximum projection depicting migration of OT-I-GFP  $CD8^+$   $T_{RM}$  cells (green) in the skin of C57BL/6J mice *in vivo* (representative of  $n=3$  mice).

**Supplementary Video 2 | Murine skin-resident  $T_{RM}$  cell migration *ex vivo*.** Confocal maximum projection depicting migration of OT-I-GFP  $CD8^+$   $T_{RM}$  cells (green) in skin of C57BL/6J mice *ex vivo* (air exposed) (representative of  $n=3$  mice).

**Supplementary Video 3 | Murine skin-resident  $T_{RM}$  cell migration *ex vivo* (non air exposed).** Confocal maximum projection depicting lack of migration of OT-I-GFP  $CD8^+$   $T_{RM}$  cells (green) in the skin of C57BL/6J mice *ex vivo* (non air exposed) (representative of  $n=1$  mouse).

**Supplementary Video 4 |  $CD8^+$   $T_{RM}$  cell migration in murine albino skin in confocal imaging.** Confocal maximum projection depicting migration of OT-I-GFP  $CD8^+$   $T_{RM}$  cells (green) in the skin of C57BL/6J albino mice, either *in vivo* (first segment), or *ex vivo* (second segment) (both representative of  $n=3$  mice).

**Supplementary Video 5 |  $CD8^+$   $T_{RM}$  cell migration in murine albino skin in MP imaging.** MP perspective top view depicting migration of OT-I-GFP  $CD8^+$   $T_{RM}$  cells (white dots indicate cells, green stripes indicate dragon tail tracks) in the skin of C57BL/6J albino mice *ex vivo* (SHG signal is depicted in blue) (representative of  $n=3$  mice).

**Supplementary Video 6 | OVA<sub>257-264</sub> recognition by OT-I-mTmG and not by gBT-GFP  $CD8^+$  skin-resident  $T_{RM}$  cells *ex vivo*.** First segment: confocal maximum projection depicting OT-I-mTmG (red) and gBT-GFP (green) cells showing steady-state patrolling behavior. Second segment: confocal maximum projection showing the rounding up and stalling of OT-I-mTmG skin-resident  $T_{RM}$  cells after OVA<sub>257-264</sub> addition, whereas gBT-GFP cells continue to patrol the skin. Green and red double-positive structures indicate autofluorescent hairs (representative of  $n=3$  mice).

**Supplementary Video 7 | OVA<sub>257-264</sub> recognition by anti-mCD8 nanobody-labeled OT-I-GFP  $CD8^+$   $T_{RM}$  cells *ex vivo*.** First segment: confocal maximum projection depicting anti-mCD8 nanobody single-positive (red) and OT-I-GFP skin-resident  $T_{RM}$  cells (green) co-stained with anti-mCD8 nanobody that show steady-state patrolling behavior. Second segment: confocal maximum projection showing the rounding up and stalling of anti-mCD8 nanobody stained OTI-GFP skin-resident  $T_{RM}$  cells after OVA<sub>257-264</sub> addition, whereas an anti-mCD8 nanobody single-positive cell continues to migrate throughout the recording (representative of  $n=2$  mice).

**Supplementary Video 8 | Migration of  $CD8^+$   $T_{RM}$  cells in healthy human skin tissue.** MP perspective top view of anti-hCD8 nanobody-labeled  $CD8^+$  skin-resident  $T_{RM}$  cells (red; white dots indicate cells, red stripes indicate dragon tail tracks) migrating in full-thickness healthy human skin biopsy; SHG indicates collagen type I positive dermis (blue) (representative of  $n=4$  individuals).

**Supplementary Video 9 | Migration of human  $CD8^+$   $T_{RM}$  cells through surrounding epidermal cells.** MP recordings showing a detailed and overview section view of anti-hCD8 nanobody-labeled  $CD8^+$  skin-resident  $T_{RM}$  cells (red) migrating amid surrounding nucleated epidermal skin cells (Hoechst, gray; SHG, blue) (representative of  $n=4$  individuals).

**Supplementary Video 10 | Migration of human epidermal CD8<sup>+</sup> T<sub>RM</sub> cells along dermal projections and in close proximity to basement membrane.** First segment: 3D surface rendering of an MP recording of an anti-hCD8 nanobody-labeled CD8<sup>+</sup> skin-resident T<sub>RM</sub> cell (red) migrating on top of finger-like dermal projections (SHG, blue) (representative of n=4 individuals). Second segment: section view and 3D surface rendering of a MP recording of an anti-hCD8 nanobody-labeled CD8<sup>+</sup> skin-resident T<sub>RM</sub> cell (red) migrating in close proximity to basement membrane (collagen type IV, green) (SHG, blue) (representative of n=3 individuals).

**Supplementary Video 11 | Migration of epidermal CD8<sup>+</sup>CD103<sup>-</sup> and CD8<sup>+</sup>CD103<sup>+</sup> T<sub>RM</sub> cells in human skin.** MP section view depicting anti-hCD8 nanobody-labeled CD8<sup>+</sup> skin-resident T<sub>RM</sub> cells (red), either negative or positive for CD103 (green), migrating through the tissue (SHG, blue) (representative of n=3 individuals).

**Supplementary Video 12 | Migration of human CD8<sup>+</sup> T<sub>RM</sub> cells below sessile Langerhans cells.** First segment: MP section view depicting anti-hCD8 nanobody-labeled CD8<sup>+</sup> skin-resident T<sub>RM</sub> cells (red) migrating in dermis (SHG, blue) and in epidermis below sessile Langerhans cells (CD1a<sup>+</sup>, green) (representative of n=4 individuals). Second segment: 3D surface rendering; third and fourth segments: section view of CD8<sup>+</sup> T<sub>RM</sub> cells migrating in close proximity to Langerhans cells (representative of n=3 individuals).

**Supplementary Video 13 | Migration of human dermal CD8<sup>+</sup> T<sub>RM</sub> cells along the perimeter of collagen type I-poor areas.** First segment: MP virtual sectioning; second segment: 3D surface rendering; third segment: perspective top view depicting anti-hCD8 nanobody-labeled CD8<sup>+</sup> skin-resident T<sub>RM</sub> cells (red) migrating along perimeter of a collagen type I-poor area (SHG, blue). Cylinders indicate tracks (representative of n=4 individuals).

**Supplementary Video 14 | Migration of human CD8<sup>+</sup> T<sub>RM</sub> cells along dermal vessels.** First segment: MP perspective view animation of full-thickness skin biopsy showing anti-hCD8 nanobody-positive T<sub>RM</sub> cells (red), and also depicting collagen type IV (green) and SHG (blue). Note that collagen type I-poor areas contain basement membrane-positive vessels. Third segment: 3D surface rendering; second and fourth segments: section view depicting anti-hCD8 nanobody-labeled CD8<sup>+</sup> (red) skin-resident T<sub>RM</sub> cells migrating along collagen type IV positive vessels (representative of n=3 individuals).

**Supplementary Video 15 | Migration of human CD8<sup>+</sup> T<sub>RM</sub> cells in and out of the dermal compartment.** 3D surface renderings and perspective side view depicting anti-hCD8 nanobody-labeled CD8<sup>+</sup> T<sub>RM</sub> cells (red) migrating in and out of collagen type I-positive areas (SHG, blue) (representative of n=3 individuals).